ELSEVIER

Journal of Power Sources 114 (2003) 137–159

JOURNAL OF POWER SOURCES

www.elsevier.com/locate/jpowsour

Influence of paste composition and curing program used for the production of positive plates with PbSnCa grids on the performance of lead acid batteries

D. Pavlov*, M. Dimitrov, T. Rogachev, L. Bogdanova

Central Laboratory of Electrochemical Power Sources, Bulgarian Academy of Sciences, G. Bonchev Street, Block 10, Sofia 1113, Bulgaria

Received 22 April 2002; received in revised form 21 August 2002; accepted 2 September 2002

Abstract

The cycle life performance of lead acid batteries with PbSnCa grids is strongly affected by the structure and properties of PAM and of the interface PAM/grid. The latter interface is formed during curing and formation of the positive plates. The processes that take place on curing of positive lead acid battery plates produced with Concast or Conroll PbSnCa grids and $3PbOPbSO_4{\cdot}H_2O$ (3BS) or $4PbOPbSO_4{\cdot}xH_2O$ (4BS) pastes are discussed in this paper. The enhanced processes of Sn and Ca segregation in the alloy of the grids during plate curing lead to the formation of a thin layer of a new phase, composed of the intermetallic compound $(Pb_{1-x}Sn_x)_3Ca$, in the spaces between the metal grains or sub-grains. This layer makes the interface heterogeneous and exerts a detrimental effect on the cycle life of the battery. In order to suppress its effect on battery performance, the thickness of this layer should be reduced by reducing the content of Ca in the grid alloy. During plate curing, the heterogeneous surface of the grid alloy is oxidized under the action of oxygen and H_2O at elevated temperature and the alkaline solution in the paste pores. A corrosion layer is formed comprising a thin sub-layer (CL1) and a thick partially hydrated lead oxide sub-layer (CL2). The 4BS/CL2 contact surface is larger and more stable than that between the 3BS particles and the CL2 layer. Both 3BS and 4BS particles are bonded to the CL2 layer through their hydrated layers. When curing is conducted at temperatures above 80 °C, 3BS particles are converted into 4BS ones which contain water. It has been established that positive plates produced with 4BS plates cured at 50 °C have the longest cycle life and adequate capacity performance, but a bit low power output. Positive plates prepared with 3BS pastes, which are then converted into 4BS ones during plate curing at 90 °C, have high initial capacity and power performance, but shorter cycle life. Batteries with plates produced with 4BS pastes and then cured at 90 °C for less than 4 h have both satisfactory power output and cycle life. The obtained results indicate that the conditions of positive plate curing exert a strong influence on the performance of batteries with PbSnCa grids.

Keywords: Lead acid battery; Lead dioxide plate technology; Curing of lead acid battery plates; Tetra-basic lead sulfate (4BS); $3PbOPbSO_4{\cdot}H_2O$ (3BS) lead–tin–calcium grid alloy structure; Hydration of 4BS or 3BS

1. Introduction

During the late 1970s, PbSnCa alloys were introduced for the production of lead acid battery grids, which reduced substantially the maintenance of the batteries during their operation. However, the life of the battery on deep discharge cycling decreased abruptly as compared to that of batteries with PbSb grids [1,2].

The following technologies have been found to improve the cycle life performance of the battery with PbSnCa positive grids:

- active block compression [3];
- addition of Sn to the grid alloy improves the conductivity of the corrosion layer [4,5];
- addition of Bi, Sb and As to the grid alloy or to the paste improve the bonds between the corrosion layer and PAM, and makes the PAM structure more stable [6];
- high charging current used in the initial charge stage [7–9];
- 4BS pastes used for the production of positive plates [10,11].

4BS pastes can be formed during two steps of the plate manufacturing process: (a) on paste preparation at temperatures higher than 80 °C [12], or (b) on curing the plates at temperatures higher than 80 °C [13]. Both methods are used in the battery industry.

The structure of the interface grid/active mass is formed during the process of plate manufacture. After pasting of the

* Corresponding author. Tel.: +359-2-718651; fax: +359-2-731552.
E-mail address: dpavlov@mbox.cit.bg (D. Pavlov).

0378-7753/02/$ – see front matter
PII: S0378-7753(02)00593-1

grids, the plates are set to curing. The grid corrodes and the obtained corrosion layer connects the grid to the paste. During plate formation, the corrosion layer and the paste are oxidized to lead dioxide.

The basic processes that take place during plate curing are: (a) grid corrosion, (b) residual lead oxidation, (c) paste recrystallization, and (d) formation of paste skeleton. It has been established that:

- during curing the corrosion layer is formed and Pb in the paste is oxidized [13–16];
- drying of the cured paste has great effect on the stability of the active mass [17];
- the phase composition of the cured paste (3BS, 4BS, PbO) strongly influences the cycle life of the positive plates [12,17–19];
- there is a linear relationship between the density of the wet 3BS or 4BS paste and the pore volume in the cured paste [18];
- basic lead carbonates formed at the PbSnCa grid/paste interface during curing exert a detrimental effect on battery cycle life [20];
- hydrothermal curing in autoclave in the presence of CO_2 and H_2O vapor improves the strength of the active material [21];
- on curing in inert atmosphere, a corrosion layer is formed as a result of H_2 evolution in the H_2O/Pb system [22].

The structures of the interfaces 4BS paste/PbSnCa grid and 3BS paste/PbSnCa grid formed during the curing process have not been disclosed up to now. It is not clear yet which is the more efficient method of 4BS paste preparation for the different types of battery applications (e.g. SLI, traction, stand by, etc.). To provide answers to these questions is the objective of the present paper.

2. Experimental

2.1. Concast and Conroll grids

The grids for the present investigation were supplied by Wirtz Manufacturing Co. Ltd. and they were produced by

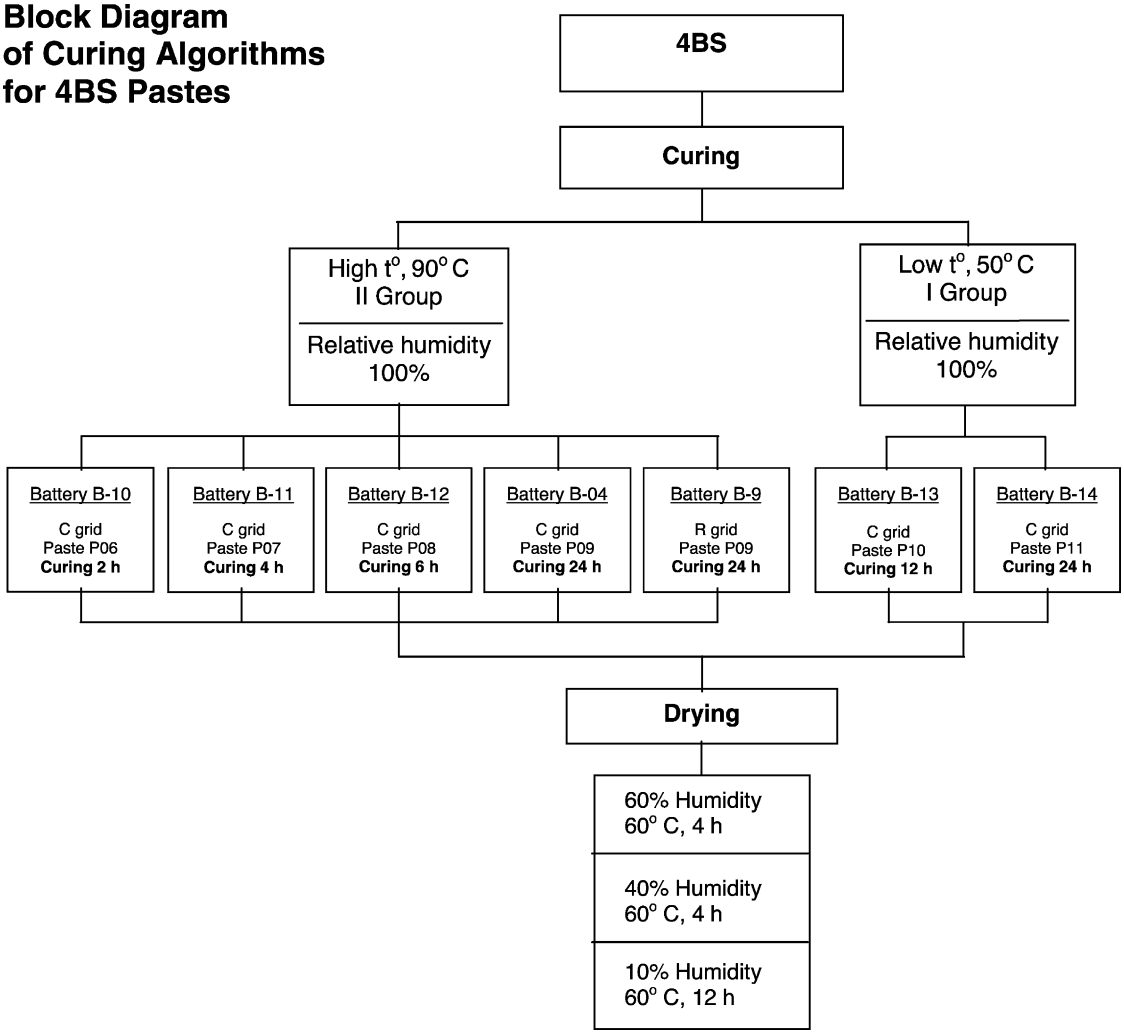

Fig. 1. Block diagram of the curing algorithms used for 4BS pastes.

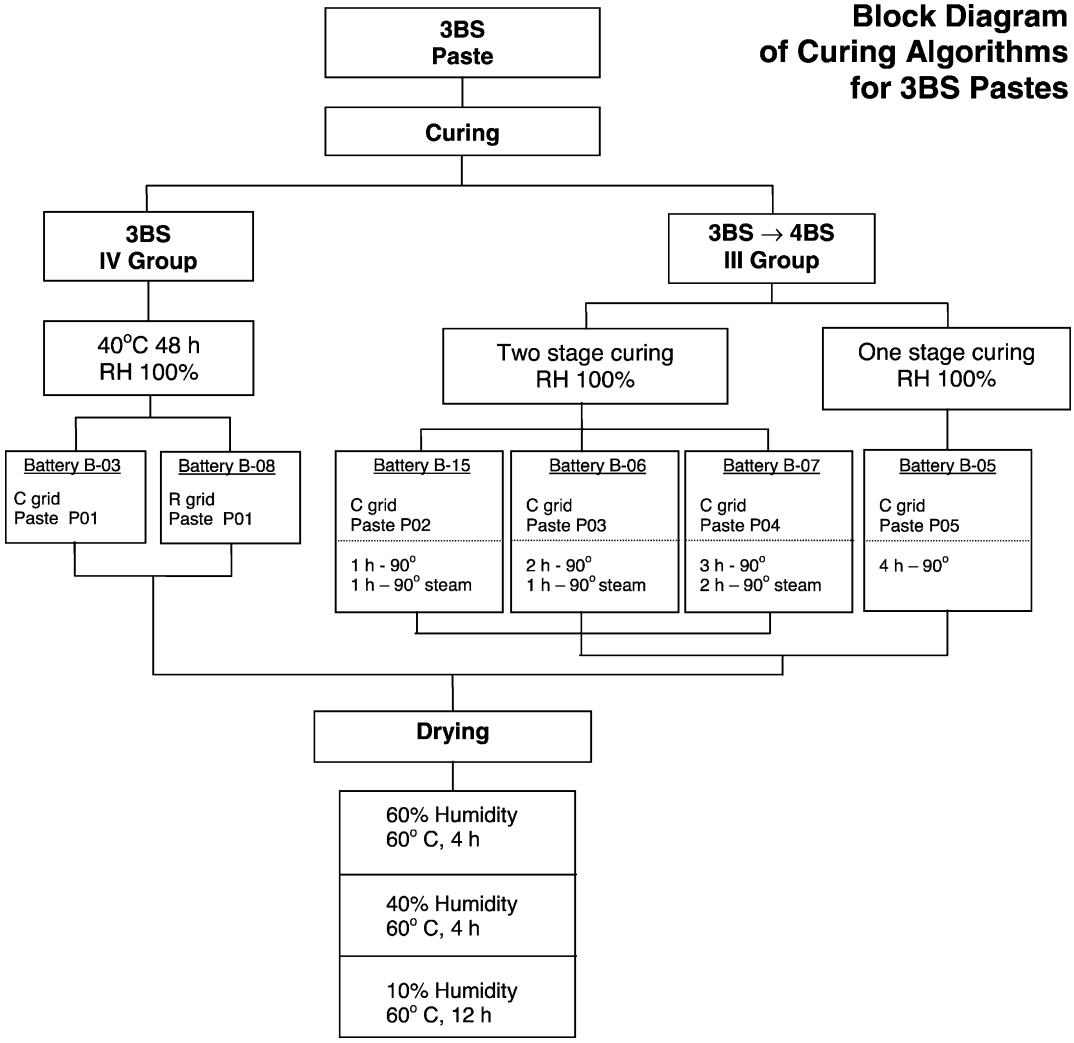

Fig. 2. Block diagram of the curing algorithms used for 3BS pastes.

the continuous casting (Concast) and the continuous rolling (Conroll) processes (denoted with C-grids and R-grids, respectively). The chemical composition of both types of grids was determined by AAS and the obtained results are summarized in Table 1.

Both types of grids have almost the same chemical composition.

2.2. Pastes and their preparation

2.2.1. 3BS paste

Five kilograms batches of paste were prepared. Leady oxide (LO, 72.72% PbO), H_2SO_4/LO = 5.0%, temperature of paste mixing maximum 50 °C, time of mixing the components 6–8 min, time of paste stirring 30 min at 50 °C.

Table 1
Chemical composition of the alloys of Concast and Conroll grids

Grid type	Sn (wt.%)	Ca (wt.%)	Bi (wt.%)	Ag (wt.%)
C-grid	1.07	0.059	0.035	0.016
R-grid	1.03	0.068	0.027	0.016

2.2.2. 4BS paste

Six kilograms batches of paste were prepared. Leady oxide (86.07% PbO), H_2SO_4/LO = 6.2%, temperature of paste preparation 92–95 °C, time of adding the H_2SO_4 solution 2 min, time of paste mixing 30 min at 90 °C, vacuum treatment [23].

2.2.3. 3BS paste for the negative plates

Six kilograms batches of pastes were prepared. Leady oxide (72.72% PbO), H_2SO_4/LO = 4%, expander UP-393 0.2%, $BaSO_4$ 0.8%, carbon black 0.2%, temperature of paste preparation maximum 50 °C, time of adding the H_2O and H_2SO_4 to the paste mixer with leady oxide 10 min, time of paste mixing 15 min at 50 °C.

A total of 13 batches of positive pastes and 14 batches of negative pastes were produced. Most of the pastes were pasted onto C-grids and only four of them were used for pasting of R-grids.

2.3. Plate curing

Figs. 1 and 2 show block diagrams of the curing algorithms used for 4BS and 3BS plates, respectively.

Five variants of curing of 4BS plates at high temperature (~90 °C) and two variants at low temperature (~50 °C) were employed. One- or two-step curing processes were used for curing of 3BS plates at 90 °C. One-step curing: the plates were placed in a chamber at 90 °C and 100% relative humidity for 4 h after which they were dried. Two-step curing: after the first curing step at 90 °C for 1 or 2 h, water steam was purged into the curing chamber and curing of the plates continued at 90 °C for a definite period of time. After curing the plates were set to drying and formation.

2.4. Batteries

The cured positive plates were mounted in cells comprising four positive and five negative plates separated by AGM separators (H&V 440 g/m^2). These cells were assembled in 12 V valve-regulated batteries, which were set to formation. After that, the batteries were subjected to capacity tests, Peukert dependence determinations and cycle life tests. The employed battery test program is presented diagrammatically in Fig. 3.

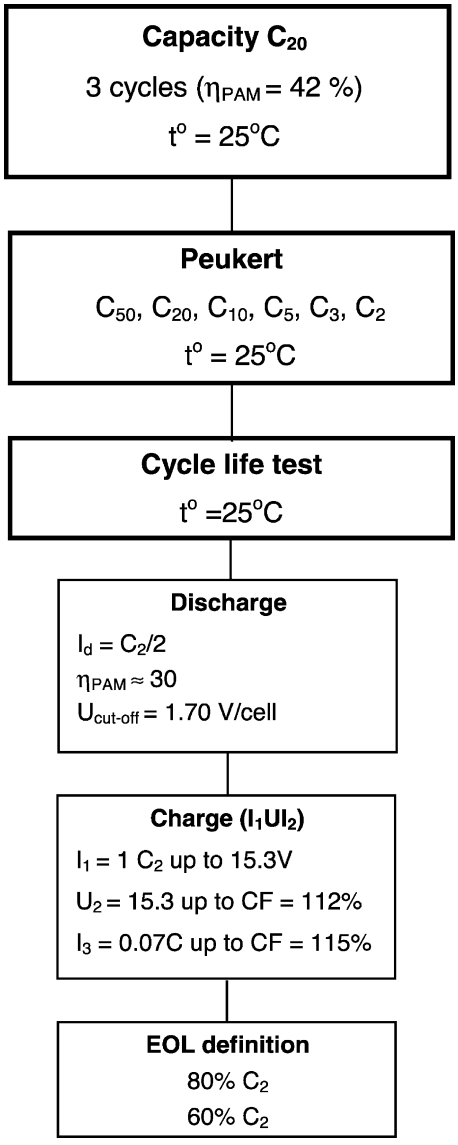

Fig. 3. Battery test program.

3. Experimental results and discussion

3.1. Grid alloy microstructure and how it changes on curing

3.1.1. Grid alloy microstructure of C and R grids before curing

Fig. 4 shows microstructures of cross-sections of Concast and Conroll grids before curing. Large-sized grains are distinguished with smooth boundaries oriented in the direction of the heat transfer during the cooling process (Fig. 4a and c). As a result of their growth the grains form a contact line in the middle of the cross-section (Fig. 4b and c). There is a more pronounced difference in grain size between the two grid surfaces of R-grids.

All micrographs evidence Sn (maybe also Ag) segregation to the sub-boundaries and grain boundaries (Fig. 4b and d). The darker zones (Fig. 4b and d) can be interpreted as defects in the structure of the grains to which Sn had segregated forming most probably phases of an intermetallic compound $(Pb_{1-x}Sn_x)_3Ca$ and an α-solid solution [24–26]. These dark zones grow from the grain boundaries towards the bulk of the grains [26].

3.1.2. Surface chemistry of the grid before curing

The elemental composition of the grid surface layer (down to 10 nm in depth) was determined through X-ray photoelectron spectroscopy (XPS). XPS measurements were carried out in the UHV chamber of the electron spectrometer ESCALAM MkII. The photoelectron lines (C 1s, O 1s, Pb 4f, Sn 3d and Ca 2p) were excited with Mg Kα radiation $h\nu = 1253.6$ eV. The surface composition was determined using normalized photoelectron intensities. All spectra were calibrated against C 1s line of adventitious carbon centered at 285 eV.

Fig. 5 presents segments of the obtained photoelectron spectra showing the above lines for a Concast and a Conroll grid.

From the line positions of Ca (347.3 eV) and Sn (486 eV) it follows that formation of CaO and SnO occurs at the surface of the grid. The binding energy values of Pb $4f_{7/2}$ for PbO and $Pb(OH)_2$ are very close, but the higher binding energy of the O 1s line (531.2 eV versus 529.7 eV for PbO), its larger width (~2 eV) and the high O 1s/Pb 4f intensity ratio (>3), favors the assignment of Pb surface species to $Pb(OH)_2$ and/or $PbCO_3$. As evident from Fig. 5, a shoulder appears on the high energy side of the C1s peak at approx. 289.2 eV. This spectral feature supports the assumption of

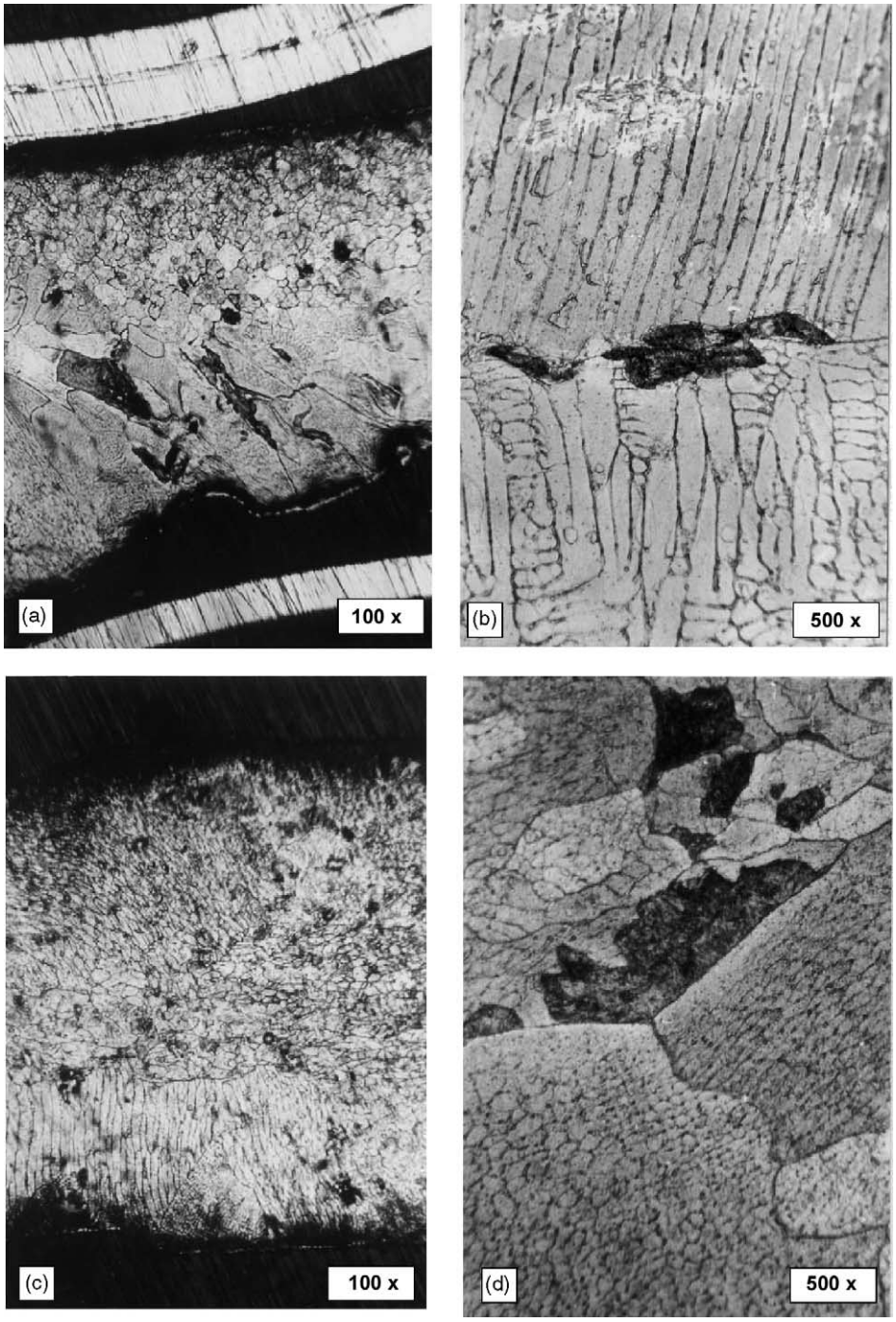

Fig. 4. Microstructure of the PbSnCaAg alloy of: (a) and (b) Concast grids, and (c) and (d) Conroll grids, before curing.

Table 2
Sn/Pb and Ca/Pb ratios at the surface and in the bulk grid alloy for C and R grids

Grid type	Sn/Pb		Sn_{surf}/Sn_{bulk}	Ca/Pb		Ca_{surf}/Ca_{bulk}
	Bulk	Surface		Bulk	Surface	
C-grid	0.0189	0.0330	1.75	0.0031	0.158	51.2
R-grid	0.0182	0.0628	3.45	0.0036	0.208	58.4

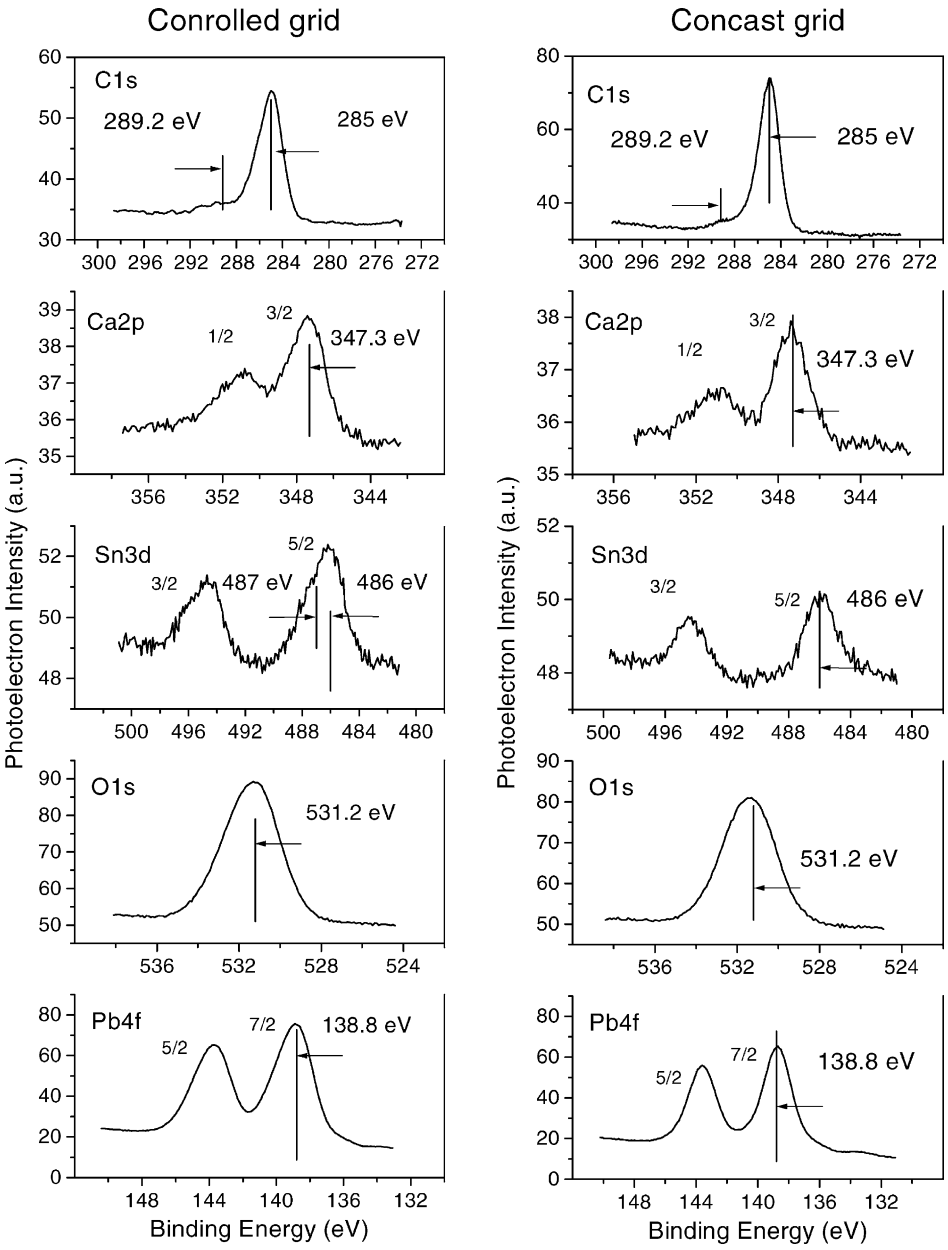

Fig. 5. Segments of the photoelectron spectra for Concast and Conroll grids as received.

CO_3^{2-} presence on the surface. A much more careful study is necessary to eliminate the possible traces of the oil vapor which may come from the vacuum pomp. Bi and Ag are not detected within the sensitivity of the XPS equipment.

Table 2 presents the Sn/Pb and Ca/Pb ratios in the grid surface layer (XPS) and in the bulk alloy (AAS) (data taken from Table 1) as well as the ratios between the Sn and Ca contents at the surface versus that in the bulk of the grid alloys.

Conclusions from Table 2 are given as follows.

- The surface layer (∼10 nm) of the R-grid contains about 3.5 times more Sn and about 58 times more Ca than does the bulk of the R-grid alloy. For the C-grid, these values are about 1.7× for Sn and 51× for Ca, respectively. During the stay of the grid in the air prior to curing Ca is oxidized forming CaO and/or $CaCO_3$ parallel to the processes of formation of SnO and PbO.
- Higher Sn, and especially Ca, segregation at the grid surface is observed with R-grids than with C-grids. Recently, Sn enrichment of surface oxide on PbSnCa grids has been proven [19] together with the formation of basic lead carbonates [20].

3.1.3. Microstructure of Concast and Conroll grids after curing of the plates

Fig. 6a and b shows the grid bar microstructure of a Concast grid and Fig. 6c and d of a Conroll grid after curing of the plates at 90 °C for 24 h. There is no essential

difference between the microstructures of the two types of grids. Curing of the plates has resulted in more homogeneous microstructures with regard to grain size (Fig. 6b and d).

Aging of the grid alloys on curing of the plates has proceeded via two mechanisms: of discontinuous and continuous precipitation, a phenomenon observed and discussed in [27,28] for alloys with Sn/Ca ratios >9. A certain ''puzzling'' at the grain boundaries is observed corresponding to irregular grain boundary movements, typical of the discontinuous precipitation (Fig. 6a and c).

The formation of a thin layer along the grain boundaries is observed, composed of $(Pb_{1-x}Sn_x)_3Ca$ and α-solid solution according to [24] (Figs. 6b and d). In addition, at the sub-boundaries and in the sub-grains, precipitations probably of the Sn_3Ca, Sn–Ag and SnPb types are formed [24,25]. As a result of the formation of all above phases, the grains and sub-grains are depleted of Sn and Ca. The presence of Ag in

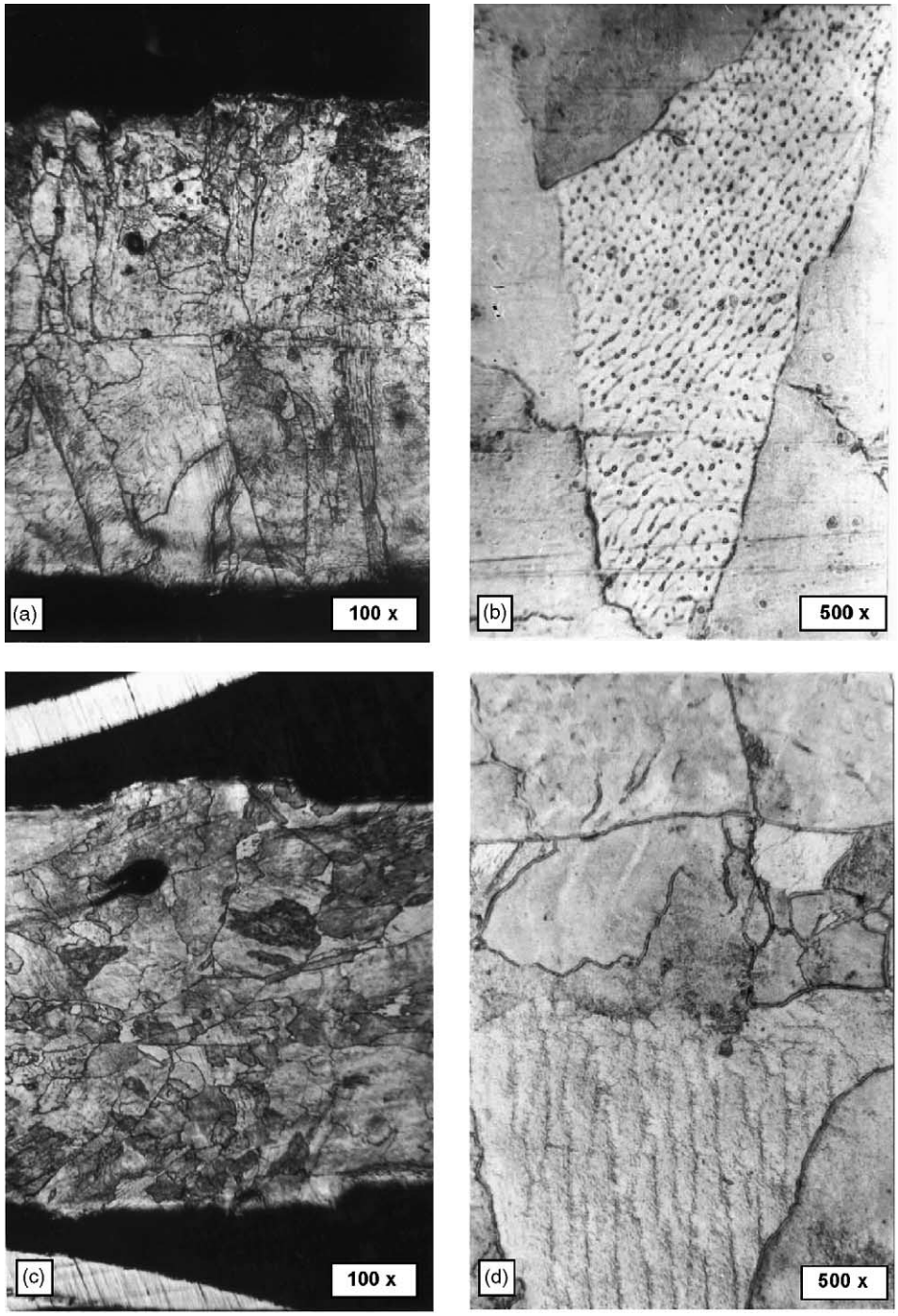

Fig. 6. Microstructure of the PbSnCaAg alloy of: (a) and (b) Concast grids, and (c) and (d) Conroll grids, after curing.

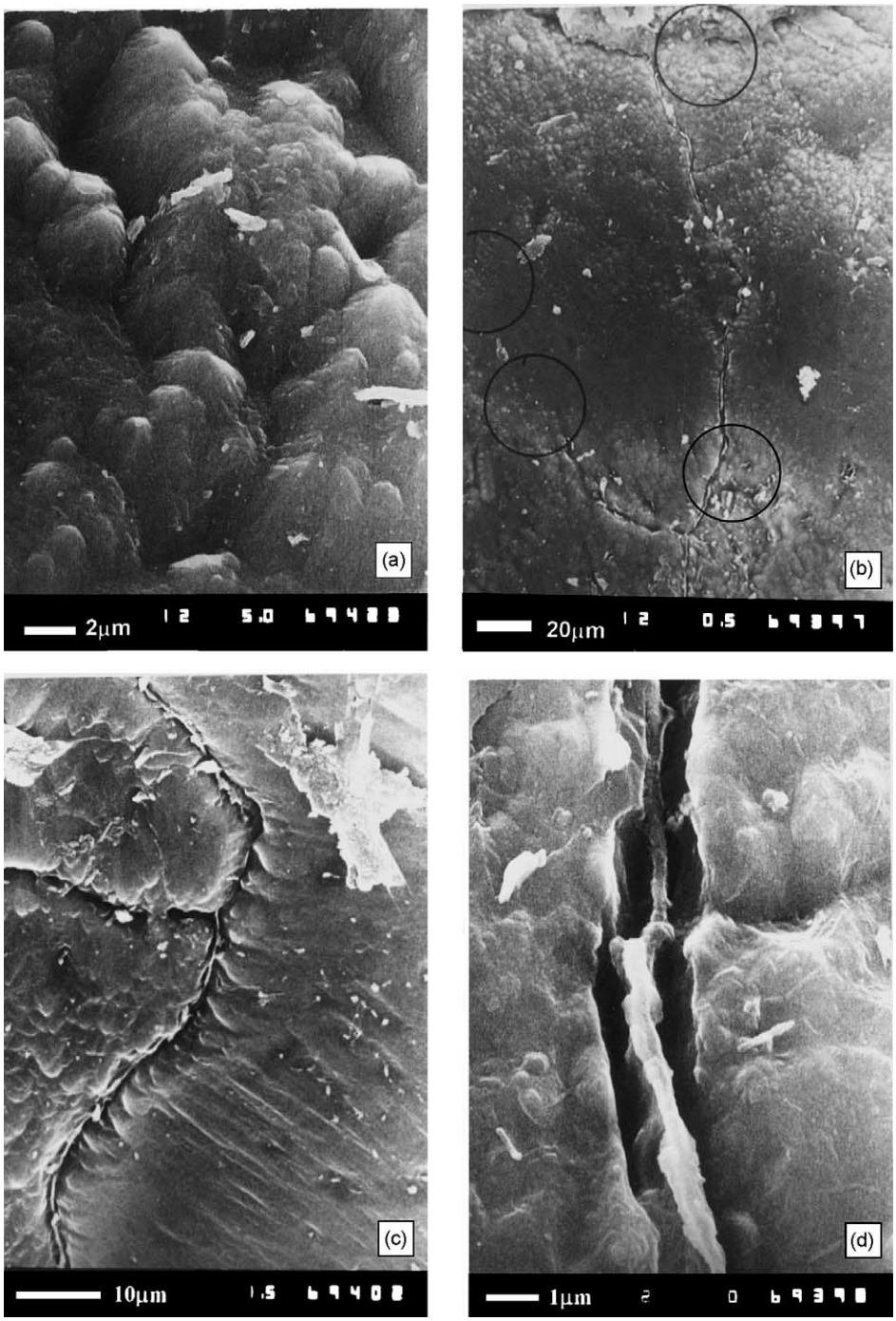

Fig. 7. SEM micrographs of the surface of the grid metal after curing at 40 °C for 48 h: (a) metal sub-grains; (b) grid surface of the cured plate, the Sn segregates to the grain boundaries; (c and d) thin intergrain layer, probably of $(Pb_{1-x}Sn_x)_3Ca$ formed during the curing process.

alloys of high Sn content impedes or slows downs the above processes of recrystallization [27].

No or small zones of intermetallic $(Pb_{1-x}Sn_x)_3Ca$ compound are observed in the grid alloy microstructure of cured grids. Most probably, Sn and Ca have diffused from these zones to the grain boundaries contributing to the formation of the thin interboundary layer of $(Pb_{1-x}Sn_x)_3Ca$.

The microstructure of the surface of a Concast grid from a 3BS plate cured at 40 °C for 48 h was observed by SEM at higher magnification. Fig. 7 shows SEM micrographs of the grid metal surface.

The sub-grains can be clearly distinguished in Fig. 7a. The closer to the sub-grain boundary the faster the metal oxidation. That is the reason for the ‘‘hilly’’ surface of the metal. Thin intergrain layers are observed between the

grains (Fig. 7c and d). The microstructure of the grid surface as illustrated by the SEM pictures can be defined as follows.

(a) Grains and sub-grains are oxidized with higher rate near their boundaries. This can be related to higher amounts of Sn and Ca caused by segregation.
(b) A thin layer formed at the grain boundaries, which is a separate phase and its composition is $(Pb_{1-x}Sn_x)_3Ca$ and α-solid solution [24]. During plate curing, this layer grows as a separate phase at most of the grain boundaries.
(c) At some grain and sub-grain boundaries (marked with circles in Fig. 7b) segregation of Sn alone occurs, which is oxidized to SnO or a solid solution of SnO + PbO is formed during curing [29,30].

3.2. Structures of the grid/paste interface formed during the curing process

3.2.1. Corrosion layer structure and its growth

In order to examine the structure of the paste/grid interface, the 4BS paste of a plate cured at 50 °C for 24 h was removed from the grid. The grid bar was slightly extended. As a result of this the corrosion layer cracked and its structure was examined. Fig. 8 presents SEM micrographs of parts of the grid bar covered with corrosion layer.

The surface of the metal grains is covered with a thin compact lead oxide film following the microprofile of the metal (Fig. 8a). This is clearly seen at the crack of the grid bar. Let us denote this sub-layer with CL1. The upper right-hand side of Fig. 8a features part of a second corrosion sub-layer (CL2) over the CL1 layer. Fig. 8b shows the structure of a CL2 layer connected with some 4BS crystals. This part of the CL2 layer has closely packed grain structure. The CL2 layer is tightly bound with 4BS crystals. The CL2 layer consists of PbO particles obtained during the oxidation of Pb. PbO particles interact with H_2O and are hydrated at the CL2/paste interface. The 4BS particles are partly hydrated, too [23]. Interaction between both hydrated layers proceeds at the contact area between 4BS particles and CL2 layer. As a result of this interaction very stable interface is formed. The last can be seen on Fig. 8b where CL2 and 4BS crystals have formed a continuous join structure. Fig. 8c presents a photograph of the interface metal/3BS paste of a cured plate. Right side of the micrograph shows metal surface partly covered by CL1 layer (white layer parts). Left side of the micrograph shows CL2 layer connected with 3BS paste particles. The thickness of the CL2 layer is 1.5–2.0 μm.

The thickness of the CL2 layer depends on the temperature and humidity in the curing chamber, the moisture content in the paste as well as on the time of curing. It is to be expected that a good paste/CL2 connection will be formed when the thickness of the CL_2 layer is commensurable with the characteristic size of the paste crystals.

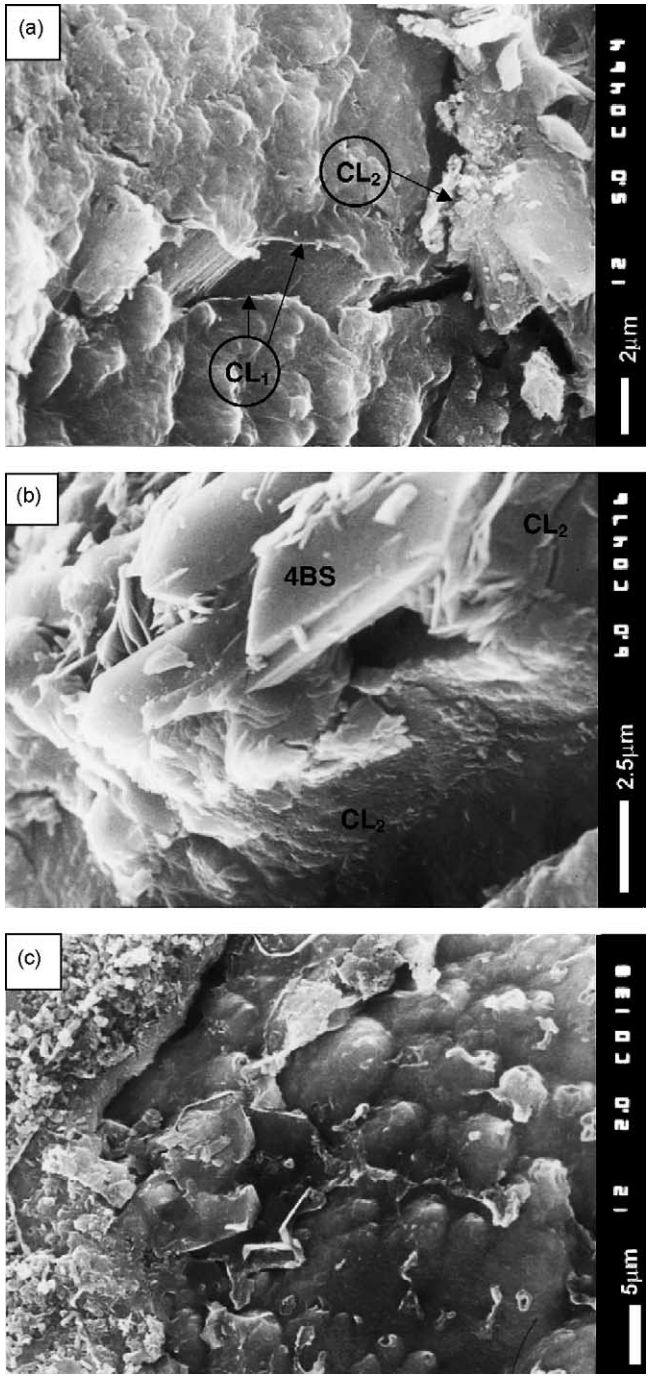

Fig. 8. SEM micrographs of the corrosion layer formed on curing of 4BS plates at 50 °C for 24 h: (a) CL1 sub-layer; (b and c) CL2 layer and its bonding to 4BS paste (b) and 3BS paste (c).

It has been established that the activation energy of the thermal oxidation of Pb to PbO is about 1 eV [31]. This low value indicates that the movement of O^{2-} ions through the oxide layer is realized by an oxygen vacancies ($O\square^{2+}$) mechanism [31]. An analogous mechanism has been found also for the electrochemical oxidation of Pb to PbO in the

lead oxide potential region [32]. An oxygen vacancies ($O\square^{2+}$) mechanism of lead grid oxidation during curing can be accepted, too. It can be presented by the following reactions:

- Pb oxidation proceeds at the metal/PbO corrosion layer interface:

$$Pb \rightarrow PbO\square^{2+} + 2e^- \quad (1)$$

- $O\square^{2+}$ vacancies and electrons move through the corrosion layer to the corrosion layer/paste interface, where they react with H_2O or O_2:

$$PbO\square^{2+} + 2e^- + H_2O \rightarrow PbO + H_2 \quad (2)$$

$$PbO^{2+} + 2e^- + O \rightarrow PbO \quad (3)$$

Reaction (2) proceeds in the hydrated $Pb(OH)_2$ part of the CL2 layer where some H_2O is intercalated.

As a result of the above reactions the corrosion layer grows. The reaction (2) of Pb corrosion with H_2 evolution was investigated in [22].

The above processes proceed in the solid phase, i.e. at a slow rate. It is known that the duration of the curing process at 30–40 °C is of the order of 48 h and about 72 h with the drying procedure included. The above processes can be accelerated if a curing chamber is used, which allows temperature to be increased to 65 °C for 3BS pastes and to 90 °C for 4BS ones, and relative humidity (RH) to be controlled. At these conditions the duration of the curing process is reduced to 12–24 h. The water loss due to the formation and growth of the corrosion layer should be compensated for. That is why a relative humidity of 100% should be maintained by introduction of water vapor in the curing chamber.

Similar processes occur on oxidation of the residual Pb particles of the paste bulk. Hence, the moisture content in the paste should be sufficiently high (8–10%) at the beginning of curing to compensate for the H_2O losses.

3.2.2. Bonding of the paste crystals to the CL2 layer

$3PbOPbSO_4{\cdot}H_2O$ and $4PbOPbSO_4{\cdot}xH_2O$ crystals contain water and are partly hydrated. PbO of the CL2 layer is hydrated, too. Curing of plates occurs at 8–10% paste moisture of the plate and temperatures of 50–60 or 80–90 °C and 100% humidity in the curing chamber. These are very good conditions for hydration of the oxide and basic lead sulfates. It can be expected that bonding between the 3BS or 4BS particles of the paste and PbO of the corrosion layer will occur by an interaction of their hydrated layers.

A SEM picture of the bonds between 4BS crystals and the CL2 layer formed in a plate cured at 50 °C for 24 h is presented in Fig. 9a. The 4BS crystals are ‘‘welded’’ to the CL2 surface at the points of contact with the latter (encircled area W in Fig. 9a). 4BS crystals, which are detached from the CL2 surface, are bonded by sinewy links to the latter (encircled area S in Fig. 9a).

Fig. 9b shows 4BS crystals at the paste/CL2 interface of a plate cured at 90 °C for 4 h. A loss of crystalline element edges and apexes is observed in the encircled zones. Rounded surfaces that are typical for hydrated substances are formed. At high temperatures 4BS crystals absorb water, forming a soft hydroxide mass, which interacts with $Pb(OH)_2$ surface of the corrosion CL2 layer. Thus, non-interrupted bonds are formed (Fig. 9b, encircled zones). Probably, the dissolved $Pb(OH)_2$ from the CL2 layer maintains the higher alkalinity of the solution in the paste pores at the interface, which facilitates hydration of the 4BS crystals.

The bonding between the 3BS crystals and the CL2 layer of the plate with C-grids cured at 40 °C for 48 h are presented in Fig. 9c. Many 3BS particles are incorporated partly into the CL2 surface layer, but their contact areas are small and, hence, it could be expected that the 3BS paste would shed more easily from the grid than the 4BS cured paste.

Fig. 9d presents a SEM picture of the interface formed as a result of one-step curing of 3BS paste at 90 °C for 4 h. The micrograph presents the CL layer looked from the side of the metal. The picture shows part of the CL1 layer (left-hand side of the micrograph), which replicates the microstructure of the metal surface. And finally, 4BS crystallites can be distinguished. They are well attached to the corrosion layer. It has been established that the slowest step in the formation and growth of 4BS crystals is their nucleation [33–35]. For the nucleation of 4BS crystals in the paste three substances should be present: 3BS, tet-PbO and orthorhomb-PbO [33]. Probably, the content of the latter compound, which is formed during paste preparation, was insufficient as a result of which only a small number of 4BS crystals had nucleated in the grid/paste interface.

3.2.3. Influence of the thin intergrain layer of $(Pb_{1-x}Sn_x)_3Ca$ on the structure of the CL2 layer

Fig. 10a presents the layer formed at the metal grain boundaries that had been incorporated into the CL1 and CL2 layers without being dissolved in them.

Fig. 10b shows the steps of oxidation of the $(Pb_{1-x}Sn_x)_3Ca$ layer and formation of hydrocarbonates. The plates with 3BS paste were cured at 90 °C for 4 h. The zone marked with the S_3 circle evidences beginning of oxidation of the $(Pb_{1-x}Sn_x)_3Ca$ layer. Probably, lead hydroxide and calcium hydroxide are formed. A more advanced stage of this process is observed in the S_2 zone, where crystallization of some oxide occurs. Well-pronounced crystals can be distinguished in the S_1 zone. These crystals look like plumbonacrites $Pb_{10}(CO_3)_6O(OH)_6$ in appearance. The pictures in Fig. 10a and b show that $(Pb_{1-x}Sn_x)_3Ca$ is formed only at some sites of the intergrain boundaries. These are the sites where the amount of segregated Ca is sufficient for the formation of a $(Pb_{1-x}Sn_x)_3Ca$ layer. At other sites where only a Sn has segregated, $Sn(OH)_2$ and SnO are formed as well as $Pb(OH)_2$.

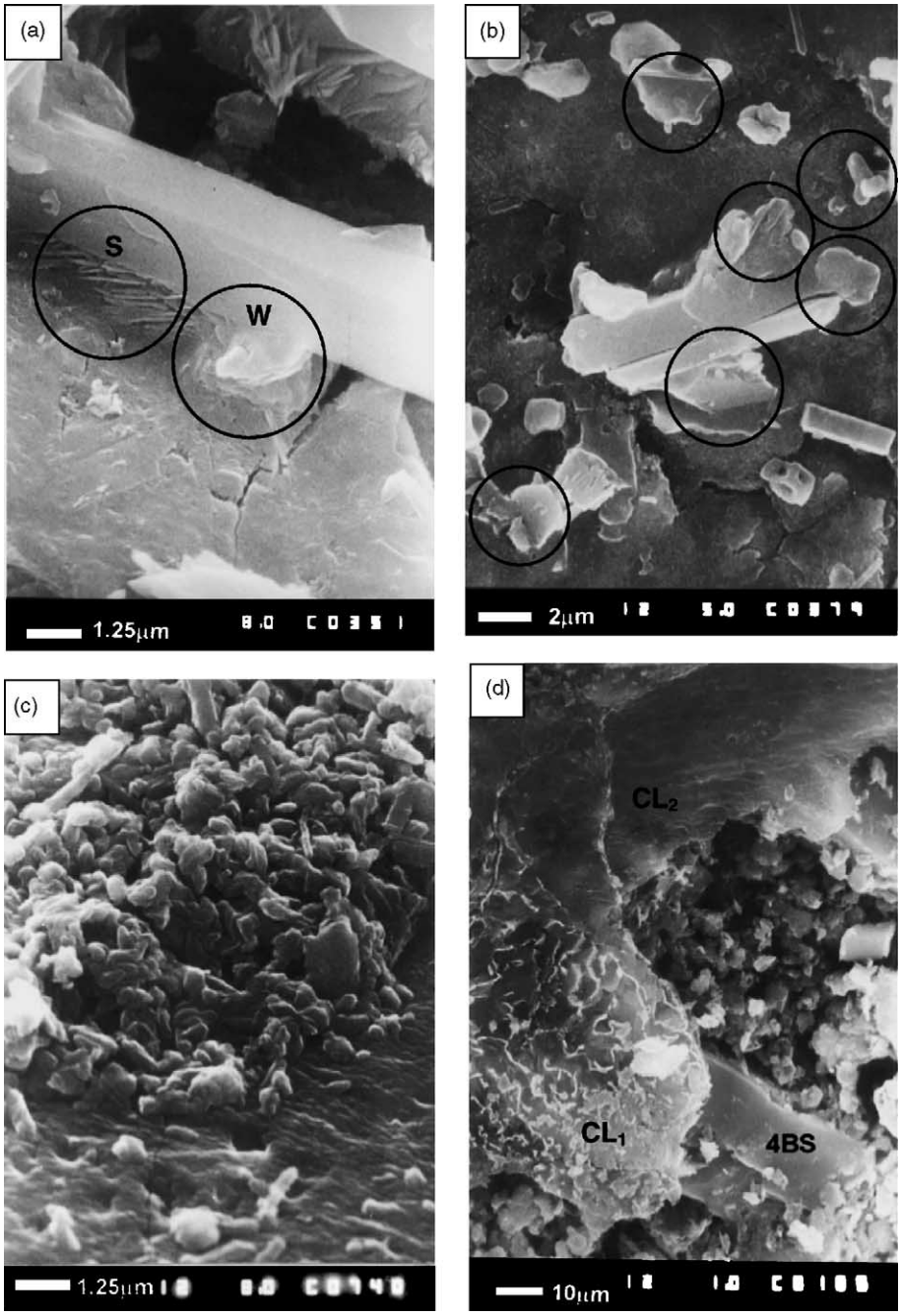

Fig. 9. Types of bonds between 4BS particles and the CL2 layer: (a) for a plate cured at 50 °C for 24 h; (b) for a plate cured at 90 °C for 4 h; (c) types of bonds between the 3BS particles and the CL2 layer for a plate cured at 40 °C for 48 h; (d) the interface formed on curing of a 3BS plate at 90 °C for 4 h. Large 4BS crystals are formed. The $(Pb_{1-x}Sn_x)_3Ca$ layer is incorporated into the corrosion layer.

Fig. 10c presents a SEM picture of the CL2 layer formed on the same plates. It can be seen that individual crystals resembling very much cerussite are formed here and there. Maybe segregation of Ca at these sites has been more intense during storage of the grids. It is oxidized by the oxygen in the air and reacts with CO_2, forming $CaCO_3$. The XPS gives some data for formation of $CaCO_3$. During curing $CaCO_3$ is hydrated. CO_3^{2-} ions reacts with $Pb(OH)_2$ forming cerussite and Ca^{2+} ions are absorbed from the paste crystals.

Fig. 10d and e shows the interface paste/CL2 layer of a plate with 3BS paste cured at 90 °C for 3 h and then treated with steam for another 2 h. CO_2 is introduced into the curing chamber with the water steam. The crystals, formed at these conditions (Fig. 10d and e), have shapes typical for the crystals of the plumbonacrite and cerussite. Obviously, the technology of 3BS conversion into 4BS through purging with water steam leads to the formation of hydrocarbonates at some sites of the paste/CL2 interface.

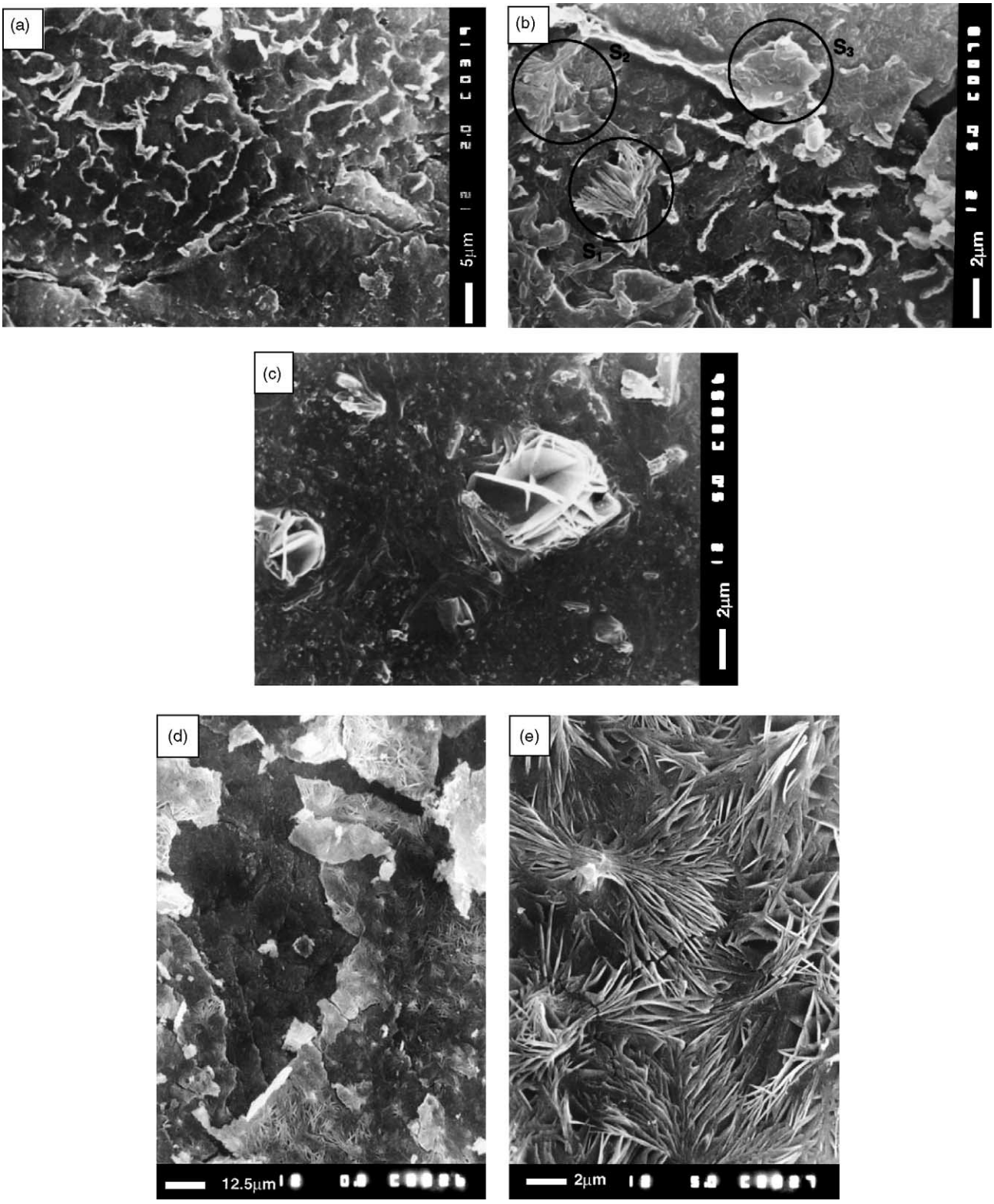

Fig. 10. (a) Structure of the thin intergrain layer of segregated Sn and Ca (the probable composition of this layer is $(Pb_{1-x}Sn_x)_3Ca$; (b) initial stages of hydration of the thin intergrain layer and formation of hydrocarbonates; (c, d and e) microstructure of the plumbonacrites and hydrocerussites formed in the paste/CL2 layer interface.

3.2.4. Formation of a gas phase at the interface paste/CL2 layer

Fig. 11 presents a SEM picture of the paste cured at 90 °C for 2 h. The 4BS crystals in the cured paste can be clearly distinguished. A certain bare grid surface area is observed. The crystals round this area are tightly packed. These bare areas on the grid surface are most probably a result of the formation of water vapour bubbles, which exert pressure on the surrounding 4BS particles and thus cause them to pack round the bubble walls. The gas bubbles are formed on heating of the plates to 90 °C. The grid metal has a lower specific heat than the paste and its temperature will rise first. The water at the grid surface evaporates forming bubbles, which displace the 4BS crystals of the paste adjacent to the grid away from the grid surface.

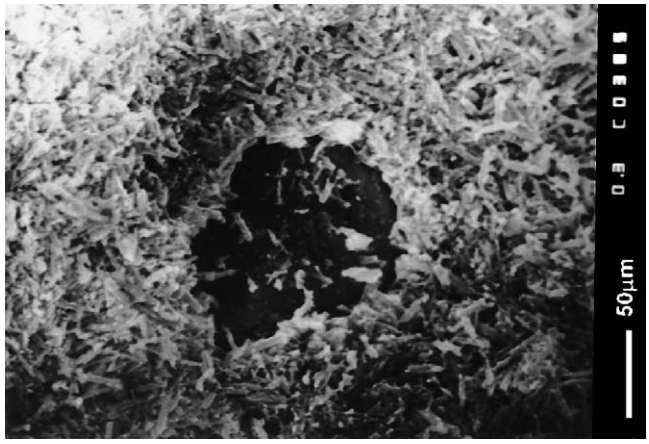

Fig. 11. Bare grid surface areas of 4BS plates cured at 90 °C for 2 h. Water vapor bubbles formed during heating of the grid have displaced the 4BS crystals and detached them from the grid surface.

3.3. Structure and properties of the cured pastes

3.3.1. Cured paste porometry

The porograms for cured pastes determined with the help of a Micromeritics AutoPore 9200 porometer are presented in Fig. 12a for 4BS cured pastes, and in Fig. 12b for 3BS pastes as well as for 3BS pastes converted into 4BS ones during plate curing.

Conclusions from the porograms are given as follows.

- In the case of 4BS pastes, only the paste cured at 90 °C for 24 h has a bit larger pore volume.
- All 4BS cured pastes have almost the same pore volume distribution by radius.
- The 3BS paste cured at 40 °C for 48 h contains fairly small pores with the largest pore volume. The pore volume versus pore radius curves for almost all pastes undergone two-step 3BS → 4BS conversion feature two inflection points, which suggests the formation of two groups of pores with pronounced average pore radius. This is related to the formation of big and small 4BS crystals, respectively.

3.3.2. Pore volume, mean pore radius, BET surface area and solid phase density of cured pastes

The obtained porometric data are summarized in Table 3.

The pore volume for seven of the cured pastes is about 0.096 ± 0.03 cm^3/g. The average pore radius values were calculated using volumetric data. Table 3 shows that the average radius does not depend on the time of curing for the Group I of pastes, whereas the BET surface increases slightly. For the Group II (4BS pastes cured at 90 °C) both the average pore radius and the BET surface increase with increasing the curing time. The 3BS paste (Group IV) has the smallest average pore radius of 0.17 µm and the largest BET surface and pore volume. The pastes subjected to two-step curing (Group III) have average pore radii varying from 0.65 to 1.25 µm and their BET surface decreases with increase of curing time.

The pastes contain a certain amount of PbO with a density of 9.3 g/cm^3 and free lead ($d = 11.3$ g/cm^3). So, the solid

Table 3
Pore volume, mean pore radius, BET surface area and solid phase densities of cured pastes

Group	Phase composition	Curing	Pore volume (cm^3/g)	Mean radius (µm)	BET surface (m^2/g)	Solid phase density (g/cm^3)
I	4BS	12 h, 50 °C	0.096	0.84	0.331	8.35
	4BS	24 h, 50 °C	0.093	0.83	0.363	8.02
II	4BS	2 h, 90 °C	0.093	0.68	0.263	8.29
	4BS	4 h, 90 °C	0.095	0.86	0.341	8.40
	4BS	6 h, 90 °C	0.099	0.89	0.363	8.09
	4BS	24 h, 90°C	0.113	0.82	0.363	7.85
III	3BS → 4BS	4 h, 90 °C	0.099	0.35	1.080	8.08
	3BS → 4BS	1/1 h steam, 90 °C	0.084	0.65	0.850	6.47
	3BS → 4BS	2/1 h steam, 90 °C	0.096	0.53	0.590	6.59
	3BS → 4BS	3/2 h steam, 90 °C	0.083	1.25	0.280	6.46
IV	3BS	48 h, 40 °C	0.110	0.17	1.620	7.97
	3BS	[35]	[35]	[35]	[35]	6.50
	4BS	[36]	[36]	[36]	[36]	8.15

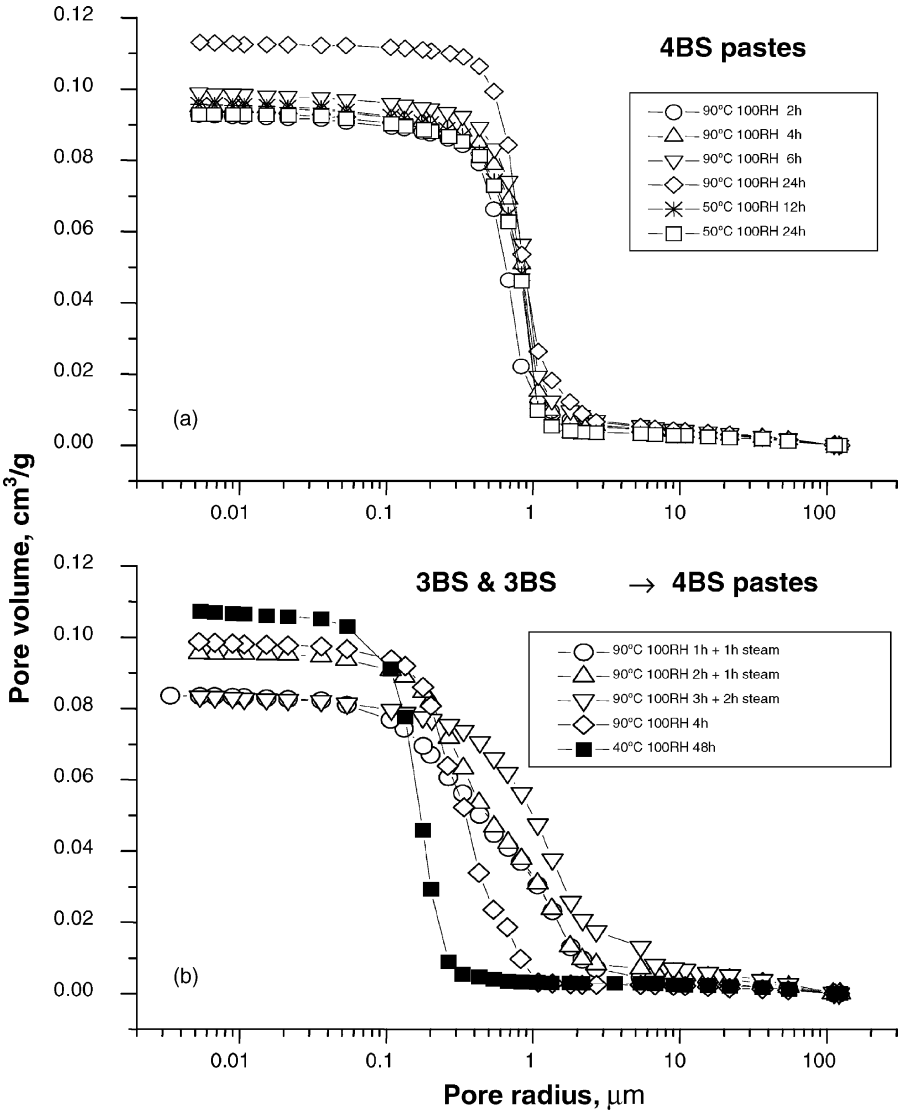

Fig. 12. Pore volume distribution by radius for 3BS and 4BS pastes cured under different conditions.

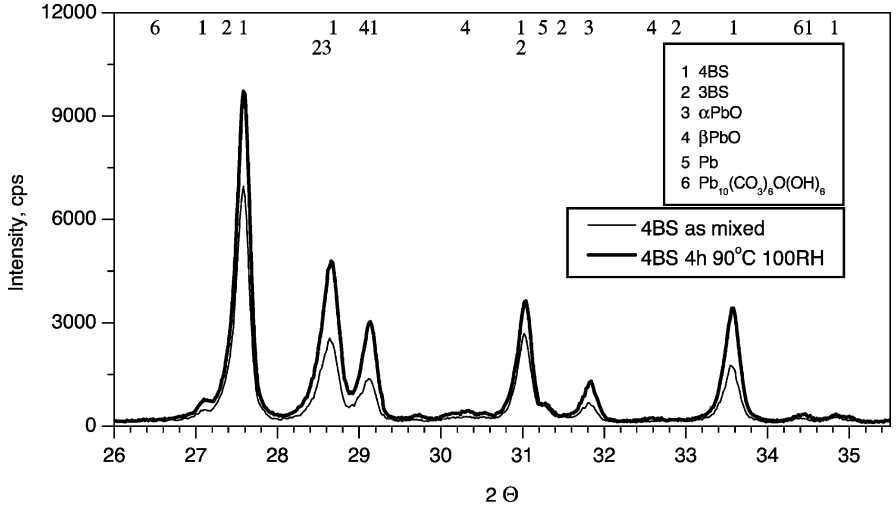

Fig. 13. X-ray diffraction patterns for 4BS pastes before and after curing at 90 °C for 4 h.

phase paste density values should be higher than those for the pure basic lead sulfate compounds.

The solid phase densities as calculated from the porometric data are presented in Table 3. The pastes can be divided into two groups: one with a solid phase density of about and above 7.9 g/cm^3 and the other one with a density of about 6.5 g/cm^3. The latter group refers mainly to 3BS pastes treated with water steam during the curing process. Though these pastes have converted into 4BS crystals their solid phase density is close to that for the pure 3BS phase.

The 3BS paste exhibits a fairy higher solid phase density than that of the pure 3BS phase (Group IV, Table 3). Such a high value can be obtained if the paste contains considerable amounts of PbO and Pb. With exception of the paste cured at 90 °C for 4 h the pastes of Group III, produced from the 3BS paste by two-step curing with steam treatment, have densities about 6.50 g/cm^3 after curing. The decrease in solid phase density indicates that the conversion of 3BS crystals into 4BS ones occurs through incorporation of water in the crystals. There is no other substance in the paste that would reduce the crystal density.

3.3.3. *Influence of curing conditions on the phase composition and the crystallinity of the pastes*

Fig. 13 presents X-ray diffraction patterns for the 4BS pastes before and after curing at 90 °C for 4 h.

The intensities of the 4BS characteristic diffraction lines increase by about 1.38 times on curing. This cannot be a result of formation of new quantities of 4BS crystals as no H_2SO_4 is introduced into the paste during the curing process. The observed changes in intensity are a result of the changed proportion between crystal and amorphous zones in the 4BS particles [23]. It has been established that 4BS particles comprise crystal and amorphous zones [23]. The crystal zones contain considerably more water. The reduced water content in the 4BS particles leads to their amorphization. Hence, during curing the 4BS particles absorb water, which results in an increase of the volume of crystal zones in them. The intensity of the characteristic diffraction line for tet-PbO is 1.83 times higher after curing than before curing, which is partially due to the oxidation of Pb.

Fig. 14 shows the changes in intensity of the characteristic diffraction lines for 4BS, tet-PbO and Pb with the time of curing of 4BS pastes at 90 °C and 100% RH.

Until the sixth hour of curing, the crystal part of 4BS particles in cured pastes features a small maximum (at the fourth hour) and decreases slightly thereafter (sixth hour). After 24 h of curing at 90 °C, substantial amorphization of the 4BS particles is observed. This amorphization affects the performance characteristics of the battery when they are determined by the positive plates.

Fig. 14 presents also the intensities of the characteristic diffraction lines for 4BS and tet-PbO for pastes cured at 50 °C for 12 and 24 h, respectively. At this low temperature 4BS particles absorb water and their crystallinity increases.

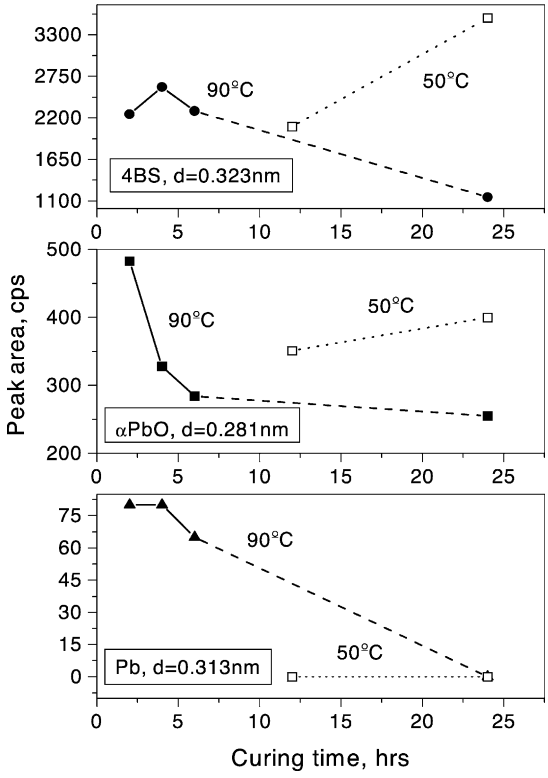

Fig. 14. Influence of the time of curing of 4BS pastes at 90 and at 50 °C on the crystallinity of the 4BS particles and on the amounts of tet-PbO and Pb in the paste.

The quantity of tet-PbO particles increases due to oxidation of Pb in the paste.

The X-ray diffraction patterns for a 3BS paste before and after curing (40 °C, 48 h) are presented in Fig. 15a.

The area of the peak ($2\theta = 27.18°$) for 3BS increases 2.43 times against a 2.44 times increase of that of the α-PbO peak ($2\theta = 31.90°$). The X-ray diffractogram in Fig. 15a evidences the presence of plumbonacrite $Pb_9(CO_3)_6(OH)_6$. The latter is formed as a result of the reaction between CO_2 from the air and $Pb(OH)_2$ from the paste during the curing process.

Fig. 15b shows the X-ray diffraction patterns for 3BS pastes cured at 90 °C and 100% RH for 4 h. Under these conditions, 3BS is converted into 4BS but only partially. The ratio between the crystal phases 4BS/3BS is 0.83.

Fig. 15c presents the X-ray diffraction patterns for the paste cured at 90 °C for 1 h and then steam treated for another hour. This paste has well pronounced 4BS crystal phase. Hence, the introduction of steam into the curing chamber facilitates the conversion of 3BS particles into 4BS ones. At this technology, some small quantity of $Pb_9(CO_3)_6(OH)_6$ is also formed in the paste.

3.3.4. *Cured paste structure and crystal morphology*

Fig. 16 presents SEM micrographs of the 4BS pastes after curing at 50 °C for 12 h. The pastes contain big 4BS crystals with smooth walls and numerous small particles in-between. Some of these small particles have formed during the

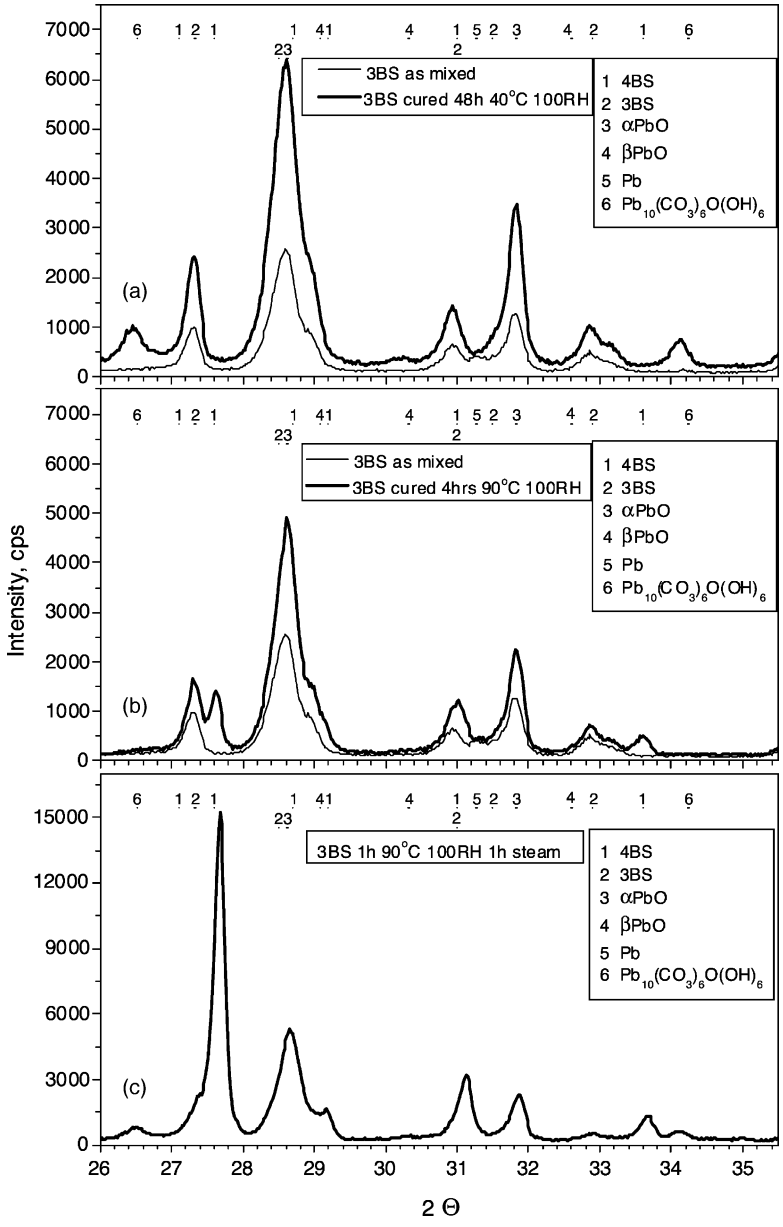

Fig. 15. Changes in phase composition of 3BS pastes on curing at: (a) 40 °C for 48 h; (b) 90 °C for 4 h; (c) 90 °C for 1 h followed by 1 h of steam treatment.

vacuum treatment of the 4BS pastes produced by the semi-suspension technology [23].

The SEM pictures of the 4BS pastes cured at 90 °C for 2, 4 and 6 h evidence very similar structure and crystal morphology to those presented in Fig. 16.

Fig. 17a shows a SEM micrograph of 3BS particles in the paste cured at 40 °C for 48 h. Individual plate-like crystals are also distinguished in the figure which are very similar in appearance to those of plumbonacrite $Pb_9(CO_3)_6(OH)_6$. The X-ray diffractogram in Fig. 15a features characteristic diffraction lines for plumbonacrite in the 3BS paste.

SEM micrographs of the paste cured at 90 °C for 4 h are presented in Fig. 17b. This micrograph presents the very beginning of the 3BS → 4BS transformation. It can be seen that some kind of substances similar to 4BS particles are formed in the paste.

Fig. 17c and d presents SEM micrographs of the paste cured at 90 °C for 2 h followed by 3 h of steam treatment. Big 4BS crystals have nucleated and grow in the paste. These crystals incorporate the hydroxides thus forming large pores round the 4BS crystals. The solid phase density of this paste is about 6.50 g/cm^3 (Table 3). 4BS particles have well shaped crystal forms (Fig. 17d). The XRD pattern for this paste indicates that there is but some amount of non-reacted 3BS.

Based on the above pictures, we assume the following mechanism of formation of 4BS crystals from 3BS ones. At 90 °C and in the presence of water in the paste pores, 3BS crystals are in a non-equilibrium state. 4BS crystals are in

Fig. 16. Paste structure and crystal morphology of 4BS paste after curing at 50 °C for 12 h.

equilibrium under the above conditions. The newly formed big particles in Fig. 17b look like hydroxides. The formation of 4BS particles in the paste may be a result of the following reactions.

First, hydration of 3BS particles proceeds:

$$3PbO \cdot PbSO_4 \cdot H_2O \xrightarrow{H_2O} 3Pb(OH)_2 \cdot PbSO_4 \cdot xH_2O$$

Hydrated 3BS particles react with lead hydroxide. When the stoichiometry of 4BS is reached, 4BS particles start to form in this strongly hydrated medium. The matrix of 4BS particles appears. The solid phase density of this paste becomes 6.5 g/cm^3 (Table 3). Fig. 17b shows that the 4BS hydrated matrix incorporates also PbO and 3BS particles. For the 4 h of curing at 90 °C, the above process is still in its initial phase. The paste contains more 3BS than 4BS (Fig. 15b) and its density is still high (Table 3). The water contained in the paste pores is insufficient for the completion of this process moreover that 4BS nucleation is a slow process [33]. That is why the pictures in Fig. 17b evidence only the initial stages of the formation of 4BS particles. In order to enhance this process, steam should be purged into the curing chamber. The micrographs in Fig. 17c and d, the XRD pattern in Fig.15c and the solid phase density of 6.5 g/cm^3 show that substantial quantity of 4BS is formed. This was actually done when curing the pastes with steam.

3.4. Influence of the curing conditions of positive plates with 3BS and 4BS pastes on battery performance

3.4.1. Initial C_{20} capacity performance

The test was performed at 20 °C with discharge current $I_{20} = 0.05C^0_{20}$. The rated C_{20} capacity (C^0_{20}) was calculated at 42% utilization of the positive active mass. The batteries were of the valve-regulated type with AGM separator. Three C_{20} capacity tests were performed first. Then the Peukert dependences were determined followed by another C_{20} capacity test.

All batteries meet the standard requirement to deliver 100% of the rated capacity during the initial cycles. The only exception is the battery prepared with 3BS plates cured at 40 °C. The rated capacities (dashed lines) and the four measured C_{20} capacity values for six batteries under test are presented in Fig. 18.

The changes in capacity give grounds for the following conclusions.

- The batteries with 3BS pastes cured at 40 °C for 48 h exhibit a decline in initial capacity performance. All other batteries, which contain 4BS pastes as originally manufactured during paste preparation or due to the conversion

Table 4
Discharge current densities yielding 80 Ah/kg PAM specific capacity and cycle life of batteries with positive plates cured by different algorithms

Group	Paste/battery no.	Grid type/phase composition	Curing	I (A/kg PAM) at 80 Ah/kg PAM	Cycle life (number of cycles)
I	083/B-13	C/4BS	12 h, 50 °C	17.77	42
	093/B-14	C/4BS	24 h, 50 °C	20.50	69
II	053/B-10	C/4BS	2 h, 90 °C	20.50	64
	063/B-11	C/4BS	4 h, 90 °C	22.00	65
	073/B-12	C/4BS	6 h, 90 °C	28.70	45
	012/B-4	C/4BS	24 h, 90 °C	25.20	49
	012/B-9	R/4BS	24 h, 90 °C	>70	48
III	043/B-5	C/3BS → 4BS	4 h, 90 °C	55.47	9
	0135/B-15	C/3BS → 4BS	1/1 h steam, 90 °C	36.05	43
	0235/B-6	C/3BS → 4BS	2/1 h steam, 90 °C	39.86	44
	0335/B-7	C/3BS → 4BS	3/2 h steam, 90 °C	43.23	34
IV	11/B-3	C/3BS	24 h, 40 °C	–	–
	11/B-8	R/3BS	24 h, 40 °C	13.77	40 (60%)

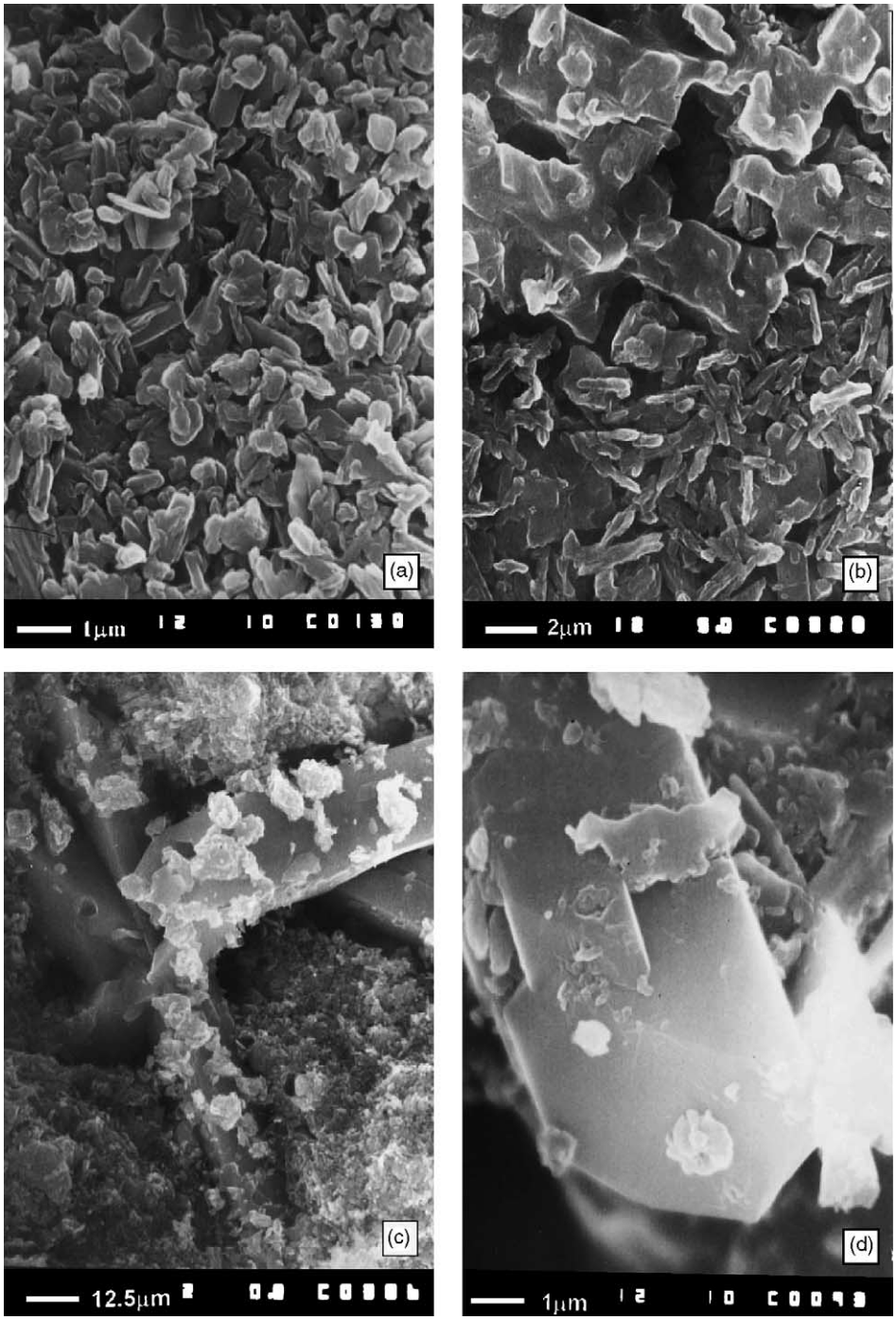

Fig. 17. (a) Structure and crystal morphology of cured 3BS paste; (b) structure and crystal morphology of 3BS paste after curing at 90 °C and 100% RH for 4 h; (c and d) structure and crystal morphology of 3BS paste (3BS → 4BS) after two-step curing at 90 °C for 3 h followed by 2 h steam treatment.

of 3BS into 4BS during plate curing, have ascending initial capacity curves.

- The batteries of Group I (4BS, 50 °C, 12 or 24 h) reach their rated capacity only at the 4th measurement.

3.4.2. Peukert dependences

Fig. 19 shows the Peukert dependences in terms of the specific capacity delivered on battery discharge with different current densities.

All batteries follow the Peukert equation

$$Q = \frac{k}{I_{\mathrm{d}}^{n-1}}$$

where the value of the exponent n being equal to 1.12.

It is evident from the figure that the Peukert curves differ for the different types of plates depending on the curing algorithm. The Peukert dependence allows predictive assessment of the power, which the plates can supply. This

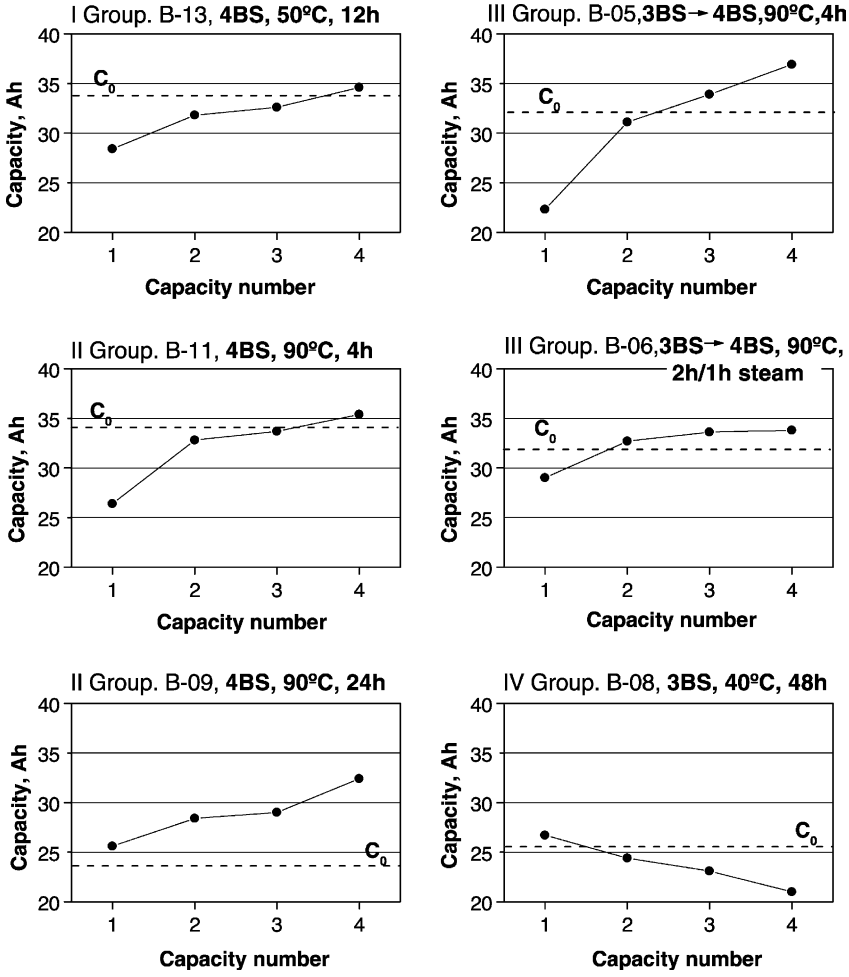

Fig. 18. Initial capacity and rated capacity (C_0) values for six batteries with positive plates cured at different conditions.

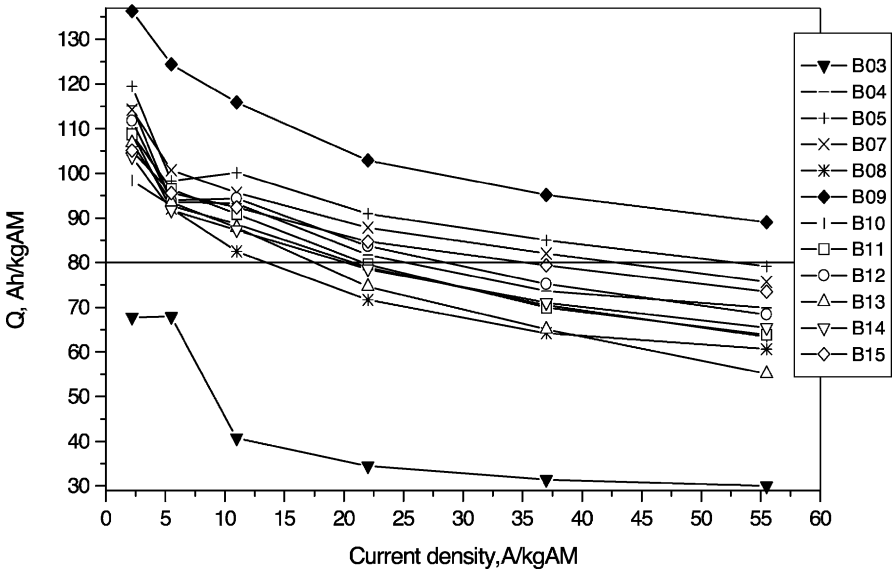

Fig. 19. Peukert dependences for the batteries under test.

can be done as follows: all batteries deliver a specific capacity of 80 Ah/kg PAM. This specific capacity is achieved with the different types of batteries when discharged at different current densities I_d. These discharge current densities I_d are presented in Table 4 and can be used for estimation of the battery power.

3.4.3. Cycle life tests

Fig. 20 presents the obtained capacity versus number of cycle curves. 80% C_{20} was assumed as the end of life limit for the cycle life tests.

The capacity of battery B-8 produced with R-grids and 3BS paste cured at 40 °C for 48 h never reached more than 75% of the rated capacity value. Battery B-5 with positive plates prepared with 3BS paste and cured at 90 °C for 4 h exhibited a cycle life of only 9 cycles, though its initial performance was very good. The cycle life data for the remaining 11 batteries under test are summarized in Table 4.

The longest cycle life has the battery with C-grid positive plates prepared with 4BS paste cured at 50 °C for 24 h (battery B-14). Battery B-13 of the same group has similar capacity curve to that of battery B-14, but its capacity declines rapidly after 40 cycles. The postmortem analysis evidenced breaking of the frames of two of the positive plates due to excessive intergranular corrosion, which had lead to failure of this particular cell. It can be expected that battery B-13 will repeat the cycle life of battery B-14.

The cycle life data and the results obtained for the discharge current ensuring specific capacity of 80 Ah/kg

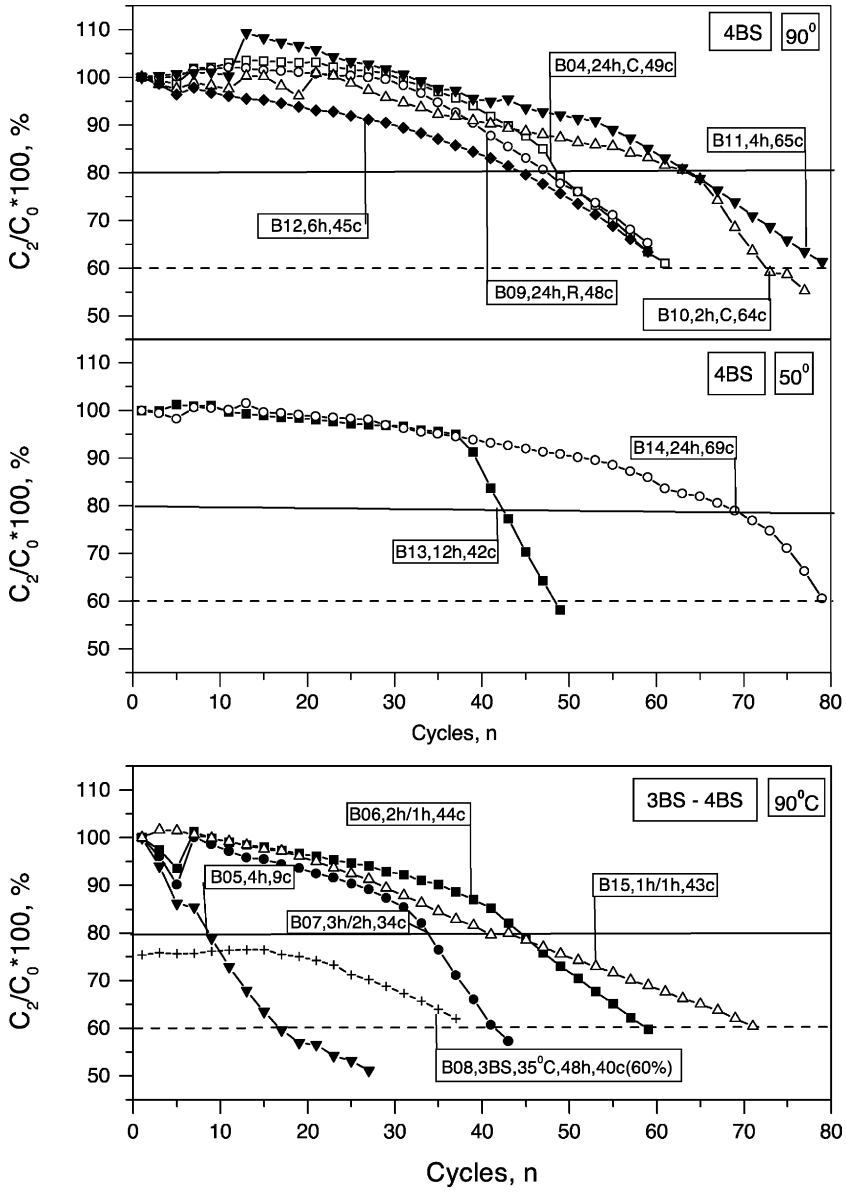

Fig. 20. Cycle life curves for the batteries with positive plates produced with 3BS and 4BS pastes and cured under different conditions.

Table 5
Postmortem analysis of the positive plates

Battery no.	Grid type/phase composition	Curing	Postmortem analysis of the positive plates	Cycle life
B-13	C/4BS	12 h, 50 °C	Frames of grids of two cells are broken by corrosion. PAM is hard only in the central zone of the plates	42
B-14	C/4BS	24 h, 50 °C	Grids are strongly corroded. PAM is hard only in the central zone of the plates	69
B-10	C/4BS	2 h, 90 °C	Grid bars and frames are strongly corroded. PAM is hard only in the central zone of the plates	64
B-11	C/4BS	4 h, 90 °C	Grid bars and frames are strongly corroded. Grid frames are broken. PAM is hard only in the central zone of the plates	65
B-12	C/4BS	6 h, 90 °C	Grid frames are broken. Corroded grid bars. PAM is hard only in the central zone of the plates	45
B-4	C/4BS	24 h, 90 °C	PAM is soft and it is not well connected with grids	49
B-9	R/4BS	24 h, 90 °C	PAM is soft and it is not well connected with grids. Parts of PAM are attached to the AGM separators	48
B-5	C/3BS → 4BS	4 h, 90 °C	PAM is not connected with grids and it is soft	9
B-15	C/3BS → 4BS	1/1 h steam, 90 °C	PAM is soft. Bad contact between PAM and grids. PAM is hard in some central zones of the plates. Thick corrosion layer	43
B-6	C/3BS → 4BS	2/1 h steam, 90 °C	PAM is soft. Bad contact between PAM and grids. Thick corrosion layer	44
B-7	C/3BS → 4BS	3/2 h steam, 90 °C	PAM is soft and it is attached to the separators. Poor grid/PAM contact	34
B-3	C/3BS	48 h, 40 °C		–
B-8	R/3BS	48 h, 40 °C	Poor grid/PAM contact. PAM is very soft and it is attached to the separators	40 (60%)

PAM presented in Table 4 give grounds for the following conclusions.

- Batteries with positive plates produced with 3BS pastes cured at 90 °C, whereby the 3BS paste converts into 4BS one, have high initial capacity and good power output performance. However, the cycle life of these batteries is shorter by about 30% than that of the batteries with 4BS (B-14, B-10, B-11).
- Batteries with 4BS plates cured at 50 °C and at 90 °C have long cycle life, but fairly low power output and initial performance characteristics.

4. Postmortem analysis of the positive plates

Table 5 presents the result of the postmortem analysis of the positive plates of all batteries under test.

According to the above analysis the batteries can be divided in three groups.

(a) Batteries with cycle life longer than 60 cycles. They have positive plates produced with 4BS paste and cured at 50 °C (12–24 h) or at 90 °C (for less than 4 h). Intergranular corrosion of the grid bars and cracking of the frames of the grids by corrosion are the basic life limiting parameter. PAM is hard in the central zone of the plates. In the periphery it is soft. The only exception from this group is battery B-13 (4BS, 50 °C, 12 h) with a cycle life of 42 cycles. The frames of two grids of this battery were broken by intense intergranular corrosion, which limited the battery cycle life.

(b) Batteries with cycle life between 35 and 50 cycles. This group includes batteries with positive plates produced with 3BS pastes transformed into 4BS during two-step curing at 90 °C, and batteries with positive plates prepared with 4BS paste and cured at 90 °C for more than 4 h. The latter has a cycle life of 48 cycles. The main problem of this group is softening of the PAM and poor contact between grid and PAM. These results indicate that the long curing time (>4 h) of 4BS plates at 90 °C is not advantageous. XRD analysis shows that these 4BS pastes are strongly amorphous.

(c) Batteries with cycle life less than 10 cycles. These have positive plates produced with 3BS paste and cured at 40 °C for 48 h (B-3 and B-8) or at 90 °C for 4 h in one step. The contact between PAM and grid is very poor. Some parts of PAM are attached to the separator. PAM is very soft.

5. Conclusions

5.1. Changes in grid alloy structure on positive plate curing

On curing at high temperature and humidity the following processes occur:

(a) enhanced segregation of Sn and Ca to the grain and sub-grain boundaries as well as to the grid surface;
(b) a thin layer of a new phase, composed of $(Pb_{1-x}Sn_x)_3Ca$, is formed in the intergrain spaces;

(c) segregation of Sn alone is observed to some grain boundaries, which is then oxidized forming a solid solution of SnO + PbO;
(d) during storage of the grids in the air before pasting, the Ca segregates to the grid surface and reacts with oxygen and CO_2 to form $CaCO_3$;
(e) The thin $(Pb_{1-x}Sn_x)_3Ca$ layer increases the rate of intergranular corrosion during grid storage and battery operation. Intergranular corrosion often limits the cycle life of the batteries.

5.2. Formation and growth of the corrosion layer as a connecting element between the grid and the paste

In the presence of water and oxygen, and at the high temperature of curing, the surface of the pasted grid is oxidized to $Pb(OH)_2$ and PbO, which form the corrosion layer. The latter consists of:

(a) CL1 sub-layer: a thin compact PbO layer, which covers the grid surface;
(b) CL_2 sub-layer: a thick granular layer of PbO and hydrated lead oxide;
(c) the thin intergrain layer of $(Pb_{1-x}Sn_x)_3Ca$ is incorporated into the CL1 and CL2 sub-layers. It is oxidized and hydrates forming heterogeneous CL2 layer;
(d) plate-like lead hydrocerussite or/and plumbonacrite crystals are formed at the CL2/paste interface as a result of the reactions between $CaCO_3$ or CO_2 from the air and $Pb(OH)_2$ of the corrosion layer;
(e) detrimental effects of:
   - intergranular grid corrosion caused by $(Pb_{1-x}Sn_x)_3Ca$ layer and
   - formation of hydrocerussite and/or plumbonacrite at the paste/CL2 interface

   could be suppressed substantially by decreasing the quantity of Ca in the alloy for example down to 0.045%.

The following processes of bonding of the paste particles to the CL2 layer have been established.

(a) 4BS particles are hydrated and thus connect to the hydrated CL2 layer. As 4BS particles are big in size, they have a large contact surface with the CL2 layer and hence a stable bond is formed between them.
(b) 3BS particles are connected to the CL2 layer through a similar process, but their contact surface is small and the interface bonds 3BS particle/CL2 layer is not strong enough.

Water in the paste/CL2 interface plays an important role in the above processes. The high relative humidity in the curing chamber can be achieved through purging water vapor or steam into the curing chamber. However, together with the steam CO_2 may also be introduced which reacts with $Pb(OH)_2$ forming lead hydrocarbonates. The latter reduce the contact surface between the paste and the CL2 layer and hence impair the paste/CL2 contact.

5.3. Paste curing

The following processes occur in the paste during plate curing.

(a) The paste particles interconnect into a continuous skeleton. This is achieved through hydration of the basic lead sulfates and lead oxide.
(b) The residual Pb from the leady oxide is oxidized.
(c) The BET surface area, the total pore volume and the mean pore radius change.
(d) When the curing temperature is about 90 °C, 3BS particles are converted into 4BS ones. This process is implemented through incorporation of a considerable amounts of water as a result of which the density of the solid phase decreases from about 8.0 g/cm^3 for 3BS pastes to 6.51 g/cm^3 for 4BS ones. This process requires the presence of steam and a minimum time of curing.

5.4. Effect of positive plate curing conditions on battery performance

Batteries with 4BS plates cured at 50 °C have the longest cycle life, but low power output and initial capacity performance. Life of these batteries is limited by the grid intergranular corrosion.

Batteries with 3BS plates cured at 90 °C, whereby the 3BS paste is converted into 4BS one, have high initial capacity and good power output, but the cycle life of these batteries is shorter.

Batteries with 4BS plates cured at 90 °C for less than 4 h have moderate capacity, cycle life and power output.

The obtained results indicate that the conditions of curing of positive plates with PbSnCa grids exert a strong influence on the performance of batteries assembled with such plates.

Acknowledgements

The present research was sponsored by The Advanced Lead acid Battery Consortium, a Program of the International Lead Zinc Research Organization, Inc. The authors want to extend their special thank also to Dr. David Prengaman for his consultations and for his efforts in arranging the delivery of Concast and Conroll grids from Wirtz Manufacturing Co. Ltd., as well as to Dr. Patrick Moseley for his support to the present work.

References

[1] K. Fuchida, K. Okada, S. Hattori, M. Kono, M. Yamaue, T. Takayama, J. Yamashita, ILZRO Project LE-276, Reports 7 and 8, International Lead Zinc Research Organization, Research Triangle Park, NC, USA, 1983.

[2] M. Dimitrov, D. Pavlov, J. Power Sources 46 (1993) 203.
[3] K. Takahashi, M. Tsubota, K. Yonezu, K. Ando, J. Electrochem. Soc. 130 (1983) 2144.
[4] H.K. Giess, in: K.R. Bullock, D. Pavlov (Eds.), Advances in Lead Acid Batteries Proceedings, vol. 84-14, The Electrochemical Society Inc., Pennington, NJ, USA, 1984, p. 240.
[5] D. Pavlov, B. Monahov, M. Maja, N. Penazzi, J. Electrochem. Soc. 136 (1989) 27.
[6] D. Pavlov, J. Power Sources 33 (1991) 221.
[7] A. Winsel, E. Voss, U. Hullmeine, J. Power Sources 30 (1990) 209.
[8] E.M. Valeriote, D.M. Jochim, J. Power Sources 40 (1992) 93.
[9] D. Pavlov, G. Petkova, M. Dimitrov, M. Shiomi, M. Tsubota, J. Power Sources 87 (2000) 39.
[10] D. Pavlov, J. Power Sources 46 (1993) 171.
[11] R.V. Biagetti, M.C. Weeks, Bell Syst. Tech. J. 49 (1970) 1305.
[12] D. Pavlov, G. Papazov, J. Appl. Electrochem. 6 (1976) 339.
[13] J.R. Pierson, in: D.H. Collins (Ed.), Power Sources-2, Pergamon Press, Oxford, England, 1970, p. 103.
[14] D.A.J. Rand, L.T. Lam, The Battery Man November (1992) 19–23.
[15] M. Dimitrov, D. Pavlov, J. Power Sources 93 (2001) 234.
[16] M.E.D. Humphreys, R. Taylor, S.C. Barnes, in: D.H. Collins (Ed.), Power Sources-2, Pergamon Press, Oxford, England, 1970, p. 103.
[17] H. Bode, Lead Acid Batteries, Translated by R.J. Brodd, K.V. Kordesch, Electrochemical Society Inc., Wiley, New York, 1977, p. 211.
[18] C.W. Fleischmann, W.J. Schlotter, J. Electrochem. Soc. 123 (1976) 969.
[19] R. De Marco, A. Rochliadi, J. Jones, J. Appl. Electrochem. 31 (2001) 953.
[20] R. De Marco, J. Liesegang, Appl. Surf. Sci. 84 (1995) 237.
[21] N. Yamasaki, J.-J. Ke, W.-P. Tang, J. Power Sources 36 (1991) 95.
[22] N.Duc. Hung, J. Garche, K. Wiesener, J. Power Sources 17 (1986) 331.
[23] D. Pavlov, S. Ruevski, J. Power Sources 95 (2001) 191.
[24] L. Bouirden, J.P. Hilger, J. Hertz, J. Power Sources 33 (1991) 27.
[25] C.S. Lakshmi, J.E. Manders, D.M. Rice, J. Power Sources 73 (1998) 23.
[26] R.D. Prengaman, J. Power Sources 95 (2001) 224.
[27] Ph. Steyer, J. Steinmetz, J.P. Hilger, J. Electrochem. Soc. 145 (1998) 3183.
[28] A. Maitre, G. Bourguignon, J.M. Florani, J. Steinmetz, J. Chanbaja, in press.
[29] A.R. Patel, D.V. Mysorewala, Mater. Res. Bull. 5 (1970) 1031.
[30] D. Greninger, V. Kollonitsch, Ch. H. Kline, Lead Chemicals, ILZRO Inc., NC, USA, 1975, p. 61.
[31] B.A. Thompson, R.L. Strong, J. Phys. Chem. 67 (1963) 594.
[32] D. Pavlov, Electrochim. Acta 23 (1978) 845.
[33] V. Iliev, D. Pavlov, J. Appl. Electrochem. 9 (1979) 555.
[34] D. Pavlov, V. Iliev, Elecrtochemistry (Russia) 12 (1975) 1735.
[35] J. Burbank, J. Electrochem. Soc. 113 (1966) 10.
[36] H.W. Billhard, J. Electrochem. Soc. 117 (1970) 690.